APPLICATIONS OF BIOLOGICALLY INSPIRED MEMBRANES

by

Eric Freeman

BSE in Mechanical Engineering, Geneva College, 2006

Submitted to the Graduate Faculty of the

Swanson School of Engineering in partial fulfillment

of the requirements for the degree of

Master of Science in Mechanical Engineering

University of Pittsburgh

2009

UNIVERSITY OF PITTSBURGH

SWANSON SCHOOL OF ENGINEERING

This thesis was presented

by

Eric Freeman

It was defended on

January 15, 2009

and approved by

Lisa Mauck Weiland, PhD, Assistant Professor

William W. Clark, PhD, Professor

Jeffery S. Vipperman, PhD, Associate Professor

Thesis Advisor: Lisa Mauck Weiland, PhD, Assistant Professor

APPLICATIONS OF BIOLOGICALLY INSPIRED MEMBRANES

Eric Freeman, M.S.

University of Pittsburgh, 2009

Nastic materials are a novel high energy density engineered membrane based on processes found in the plant kingdom. These membranes are engineered using biomimetic principles using protein transporters extracted from beet cells. These embedded transporters are capable of producing work through pumping fluid across the membrane (dependent on concentrations and fuel availability). Through this process, they may also produce controllable bulk deformation through the establishment of an osmotic gradient.

Current experimental testing has been focused largely on a cylindrical setup, where the membrane is stretched across one side of a barrel apparatus. To determine the total potential of the nastic material, a spherical set up must be examined, which is costly to create in a laboratory environment. To determine the worth of the spherical model, a computational model was created using transport principles examined by Endresen et al.

This model will be examined and modified to simulate a wide variety of conditions. Through careful evaluation of the results, data for actuation properties and model performance based on inputs and conditions will be obtained. This data will assist in determining the overall capabilities of the nastic material, and will aid future research. Finally, alternate uses for the nastic materials will be explored and discussed.

TABLE OF CONTENTS

LIST OF TABLES

LIST OF FIGURES

ACKNOWLEDGEMENTS

1.0   OVERVIEW

Biomimicry, a relatively new science that looks to naturally occurring systems in biology for inspiration in new technology is of particular interest in solving complex engineering problems. One current challenge is developing a tailorable smart or active material that is capable of rapid change through external stimulus.

Initial goals for this study were to create a flexible morphing membrane for aircraft to allow change in wing shape during flight. Plants possess the ability to achieve bulk deformation through the controlled flow of fluid and charge across their cell membranes in a process called nastic movement. This mechanic would be useful in a variety of applications, ranging from actuation to pharmaceutical delivery.

Engineered nastic membranes consist of a bilayer membrane with embedded proton pumps and various transport proteins. Adenine triphosphate (ATP) is introduced to the membrane, which activates the proton pumps which moves select ions against the electrochemical gradient into an inclusion. The resulting electrochemical imbalance then activates the cotransporters and exchangers, which move the ions back out of the inclusion along their respective electrochemical gradient and use the downhill motion of the ions to move fluid uphill into the inclusion. This results in the expansion of the nastic inclusion until the osmotic pressure is cancelled out by the hydrostatic pressure and equilibrium is achieved.

To predict this behavior a model based on the equations derived by Endresen et al. on transport kinematics was created. This model consists of two parts – a hyperelastic surrounding

1

polymer matrix that allows fluid flow and the membrane containing the transport proteins. The outer polymer matrix is modeled through ABAQUS using the Mooney-Rivlin equation, and the transport process itself is modeled through equations derived by Endresen based on reaction kinetics. These two components are coupled together in the user-defined program, which uses numerical methods to solve the stiff system of differential equations and calculate the behavior of the nastic material over a period of time. Experimental research performed by Sundaresan and Matthews was used to verify and calibrate the computational model for a cylindrical case which examined stretching the nastic membrane across the base of a cylindrical inclusion. Once the model was calibrated with these results, the model was adapted to model the case of a spherical inclusion, which is akin to the inclusions found in nature.

Nastic materials were created initially to explore the viability of an engineered bio-inspired actuator. To determine the capabilities of these nastic inclusions the model was adapted to various conditions, such as variations in the amount of available ATP, changes in the membrane properties, changes in the geometry of the inclusion itself and constrictions on sides of the polymer matrix. These studies provided information on the actuation properties of the nastic inclusion and from them values for impedance matched work for varying inclusion conditions and geometries were estimated. The results suggested that an engineered nastic material may be worthy of further development.

Nastic materials are still a new phenomenon, and their versatility is still being considered. One such application is that of pharmaceutical drug delivery, which will be introduced in this thesis. Due to their unique on-trigger expansion behavior, nastic inclusions may be ideal for targeted vaccine delivery as opposed to traditional anti-biotics which rely on a time dependent

dissolving of the external shell. The preliminary studies were performed. These studies suggest that on-demand control of pharmaceutics release may be achievable.

2.0   LITERATURE REVIEW

2.1 SMART MATERIALS

Actuators translate an applied stimulus such as heat, light, or current into a controllable force and motion. This broad definition applies to transducers such as electric motors, many biological systems such as muscles and plants, and "smart" (or "active") materials. A smart material has as an intrinsic property the ability to transform energy from one energy domain to another; for instance, an electromechanical smart material can convert an electrical stimulus into mechanical deformation. Reports of energy transduction in some materials date back to the 1800s (Curie 1887). For about a century this phenomenon was regarded as little more than a quirk in nature. However, in the 1980s sincere interest arose in utilizing smart materials in the creation of adaptive structures. Through electronics, these smart structures have been refined and now redefine the concept of structures from a conventional elastic system to an adaptive and active structure, capable of sensing, controlling, and responding to stimuli. (Tzou, 2004)

A smart material may be employed to create an adaptive system that is actively smart in regards to sensing and actuating functions. Examples include windshield wipers that sense and respond accordingly to the amount of rain falling on a windshield, or a braking system which alters the damping according to the road conditions for better control. In general smart materials applications fall into several categories. They may be used in sensors, actuators, structures, mechanical systems, medical and biomedical applications, mechatronic systems, and finally

smart structures and structronic systems. (Newnham, 1992)   In this thesis the focus is predominantly on a novel biomimetic smart material that will enable development of smart structures and structronic systems such as adaptive structures and composites, shape control, adaptive aircraft wings, and self-sensing actuators.

But what defines a "smart" material? A material cannot be truly intelligent. Smart refers to the passive smartness, or the ability to respond to environmental conditions in a useful manner. Some attributes of this passive smartness are:

Selectivity	Shapeability	Stability and Multistability
Self Tuning	Recovery	Survivability
Sensitivity	Elegance	Adaptability

One of the first observations of coupled (smart) material response was reported 1880 by the Curie brothers. They found that electric fields were generated when forces were applied to quartz crystals, and dubbed the effect piezoelectricity. This concept of converting force into current (or vice versa) now guides the use of piezoelectric materials in sensor applications and precise actuation applications. Now a range of piezoelectric materials are integrated in adaptive structures and microelectromechanical systems in applications such as robotics, vibration controls and isolations, thin-film MEMS, health-monitoring, and many others. (Tzsou, Lee, Arnold, 2004) Moreover, modern smart materials also encompass an array of coupled response materials including but not limited to thermomechanical shape memory alloys and polymers, optomechanical fiber optics, and pyroelectric infrared materials.

In the case of smart materials that couple to the mechanical domain and subsequently employed as actuators, the properties of blocked force and free displacement are of considerable interest. Blocked force is the amount of force generated when the material is mechanically constrained in the direction of motion for a specified level of stimulus. Free Displacement is the

maximum displacement reached when the material is allowed to freely expand for the same stimulus. Together these values enable identification of the Impedance Matched Work which may be achieved at the specified level of stimulus.

Impedance Matched Work is often employed as a benchmark with which compare to various smart materials for a given application, and therefore warrants further discussion. In order for the smart material (or any actuator) to do work there must be a load present, against which work is done. Consider the case of a smart material working against a spring. If the spring is infinitely stiff, then upon stimulation the smart material will generate the maximum possible force (blocked force F_b), but no displacement. So no work will be done. At the other extreme if the spring has no stiffness then the maximum possible displacement will be achieved (free displacement δ_{free}), but no force will be developed. So again, no work will be done. Varying the spring stiffness between these extremes will result in varying levels of work being performed with the maximum occurring at the midpoint as illustrated in Figure 2-1. The area under the curve illustrated is the impedance matched work and is given by:

$$W = \frac{F_b \delta_{free}}{8}$$
(2-1)
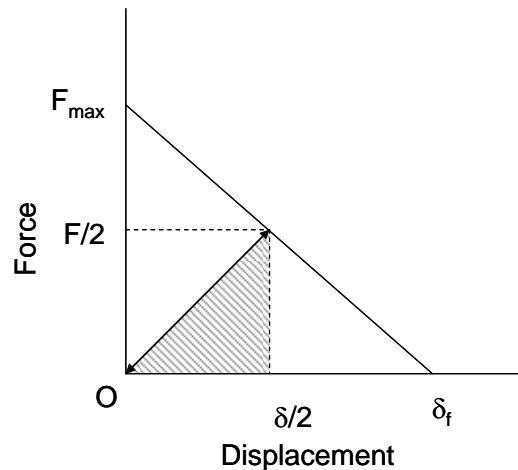
Figure 2-1 - Illustration of work related to free displacement and blocked force

6

2.2 NASTIC MATERIALS

The smart material of interest in this thesis is biomimetic – or life imitating. Biomimetic and bio-inspired studies have recently drawn considerable attention as potentially offering viable strategies to improve current technology. This methodology approaches nature itself as a large database of already existing solutions to difficult problems. Through studying how various naturally occurring systems adapt and optimize themselves to deal with a variety of obstacles, it may be possible to apply these same principles to engineering applications. One common example from the animal kingdom is the study of Gecko's toes, and their ability to stick to any surface yet still retain mobility (Autumn et al. 2006). Alternatively, there are also a number of examples from the plant kingdom. For instance, despite the absence of a muscular system, plants are able to turn toward the sun. Similarly plant tendrils are able to locate and affix themselves to nearby structures. These types of movements are collectively referred to as "Nastic Movements."(Sundaresan, Leo, 2006) A more dramatic example of nastic movement is the controlled deformation observed in the venus fly trap. This plant uses controlled turgor pressure to snap its petals shut and capture potential meals. The requisite turgor pressure arises from controlled transport of fluid and ions into/out of specific regions within the plant; the resulting differential swelling/collapse of neighboring regions in the petals enables movement. If this phenomena can be duplicated it may be possible to build microscale biological actuators with a variety of engineering applications. The following thesis provides a quantitative study of the transport proteins responsible for nastic movements and their subsequent active effect on the host environment.

Figure 2-2 illustrates the basic biological components responsible for the nastic movements just described. The figure illustrates the four basic biological transport proteins penetrating the surface of an enclosure. With the appropriate stimulus these proteins behave in much the same way as a system of hydraulic pumps and valves. Such a system could pump the enclosure into a state of expansion or collapse. A more detailed description of the system is as follows.

There are four basic biological transport protein categories: channels, pumps, exchangers and cotransporters. The pumps use the biofuel ATP (adenine tri-phosphate) to move protons across the membrane against their electrochemical gradient. The gated channels allow for passive diffusion of fluid and select ions across the membrane with a stochastic gating behavior. The exchangers and cotransporters use the energy gained from moving one ionic species along its preferred gradient to move a separate ionic species against its gradient. Cotransporters move both species in the same direction, while exchangers move the species in opposite directions. Both of these proteins move the species simultaneously – *viz.*, the exchange will not occur unless both species are present.

Some or all of the transport protein types may be found in any one system. Within a given system, the proteins penetrate a lipid bilayer membrane which surrounds an inclusion. The membrane itself is also permeable to small ions, and thus diffusion may occur.
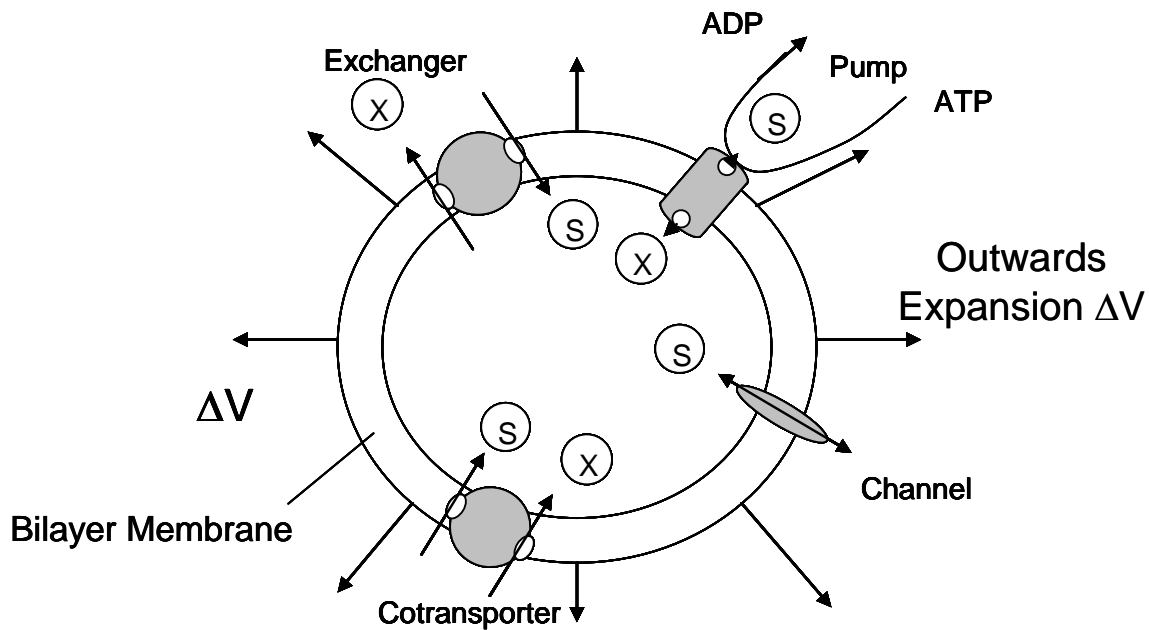
Figure 2-2 - Illustration of Biological Transport (s and x are ionic species)

One method of initiating the deformation of the inclusion is through the introduction of ATP, which activates the proton pumps. These pumps move protons across the membrane into the inclusion, which results in an electrochemical imbalance. This imbalance then triggers the exchangers and cotransporters which move the protons back out of the inclusion and in turn pump an alternate chemical species into the interior. If the channels are gated or impermeable to this species, water diffusion through the membrane will begin to offset the chemical imbalance. The inclusion will expand. This expansion will continue until the increased membrane load opens the channels and/or the chemical imbalance is neutralized. Introduction of an alternate external stimulus such as pH change or in some instances simple removal of the ATP stimulus reverses the process. Thus an actuator has been created.

Many inclusions may be arranged in an array as illustrated in Figure 2-3. Location specific stimulus may be used to expand some inclusions at the expense of others. This fundamental trigger also allows the venus fly trap to capture an insect. The inclusions will be imbedded in a polymer matrix which provides a sort of backbone for the array while remaining permeable to the required fluids. This vision is also the driving force for nastic active materials developments.
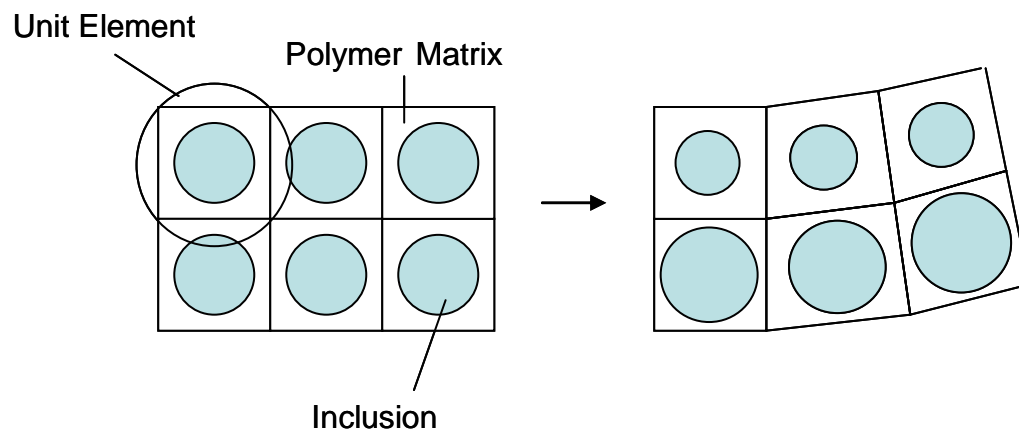
Figure 2-3 - Array Deformation

In order to control this type of system a number of challenges must be met. Some efforts have focused exclusively on mimicking the controlled expansion/contraction of selected regions within a material array with relatively simple hydraulic stimuli (no biological transport proteins). Other efforts have focused almost exclusively on the biological transport proteins with the long term intent of directly mimicking nature. Following is a review of nastic mimicking efforts to date.

2.2.1 Early Applications

Initially these engineered nastic materials were intended for use in creating a flexible outer skin for aircraft. This research effort was funded by DARPA to explore the potential of several smart materials for creating an outer skin to allow rapid shape change while maintaining structural integrity.   In one effort the inclusions were to be placed in a series of flattened tubes. As fluid was pumped into the inclusions, these tubes would inflate and provide force generating capabilities. However, as the inclusions expanded the angle of the cell wall changed, the inclusion became a cylinder and the resultant force was reduced as the contact surface area was decreased. While initial tests demonstrated that this nastic approach provided enough tensile force to support aerodynamic loads, the materials were unable to be produced at the scale required for tensile skins. In addition, the displacement was too limited, and further calculations showed that the approach would suffer from slow reaction times and required more support hardware than mass limitations would permit. (Cadogan, Smith 2004).

2.2.2 Transport Modeling – Nastic Proof of Concept

Sundaresan and Leo were responsible for the early experimental studies determining the capabilities and mechanics of the nastic membrane. They found that mass transport for actuation could be generated through one of three methods:

1. utilizing an ATP stimulus with an active transporter (a pump) to transport ions and neutral species with water molecules;

2. utilizing a chemical or electrical stimulus with a secondary active transporter (a cotransporter) to move a select species with water molecules; or

3. utilizing a combination of ATP + active transporters (pumps), and secondary active transporters (cotransporters) in which the former provides the the stimulus for the latter. (Sundaresan & Leo, 2008)

These studies resulted in the creation of a prototype actuator which relied on the secondary active transporter. In the prototype a phospholipid bilayer membrane was suspended across an artificial, porous substrate at the base of a series of cylinders as illustrated in Figure 2-4. The transport proteins were then introduced and allowed to self-assemble through the thickness of the phopholipid membrane. The transport proteins selected were SUT4 sucrose cotransporters which respond to both sucrose and protons (or pH gradients). The cylinders were filled with fluid of a fixed pH, and then the assembly was placed in a fluid reservoir with a different pH.   The pH gradient resulted in activation of the transport proteins, and subsequently transport of fluid, sucrose, and ions against gravity. This proved that the engineered nastic material was capable of performing work. The next step was to model and examine the mechanisms driving the transport.
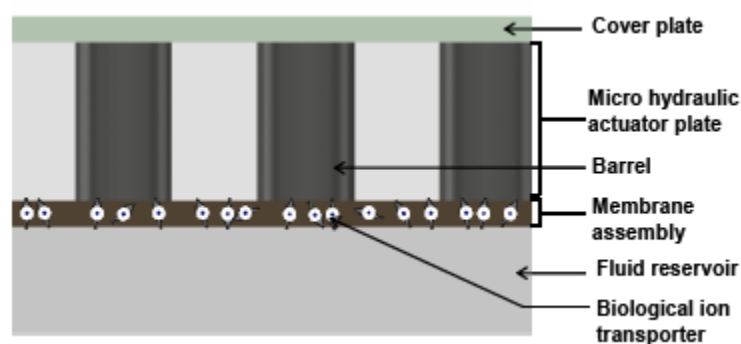
Figure 2-4 – Chemomechanical Actuator [SUNDARESAN, LEO, 2005]

It was next necessary to develop a quantifiable understanding of the observed response; for instance, how to confirm that the SUT4 cotransporters had successfully self-assembled on the

12

membrane and were in fact responsible for the observed response? A series of control tests were performed, wherein it was established that membranes that had not been subject to the SUT4 penetration step were unable to transport fluid against gravity. In addition, it was observed that these membranes displayed higher electrical impedance than those subject to the SUT4 penetration step. Thus, through approximating the biological layer as an electric circuit, an equation was created to model the observed electrical impedance across the layer, where R+jX is the impedance, G_m is the parallel admittance, ω is the frequency of the applied voltage, and τ_m is the ratio of the parallel capacitance and parallel admittance.

$$R + jX = \left\{ R_l + \frac{1}{G_m\left(1 + \omega^2\tau_m^2\right)} \right\} - j\left\{ \frac{\omega\tau_m}{G_m\left(1 + \varpi^2\tau_m^2\right)} \right\} \tag{2-2}$$

Prior to this series of experiments selective transport through the SUT4 was not well understood, but the experiments showed that adding purified SUT4 cotransporters to the phospholipids mixture on the porous substrate enhanced the amount of volume change in the barrels (Sundarsan, Leo 2005). Nastic actuators were experimentally achievable.

In future research, Sundaresan and Leo refined the chemomechanical transporter. Sucrose and proton ion fluxes through the membrane due to applied concentration gradients were determined through phenomenological equations developed by Kedem and Katachalsky (1961) and Katachalsky and Curran (1965).

$$\phi_s = L_{s,s}\Delta\mu_s + L_{s,p}\Delta\mu_p \quad \phi_p = L_{p,s}\Delta\mu_s + L_{p,p}\Delta\mu_p \tag{2-3}$$

where ϕ represents the proton and sucrose fluxes, c is the concentration on either side of the membrane, and μ is the chemical potentials for the two,

$$\Delta\mu_p = RT\ln\left(\frac{c_1^p}{c_2^p}\right) \quad \Delta\mu_s = RT\ln\left(\frac{c_1^s}{c_2^s}\right) \tag{2-4}$$

In the above expressions L represents the coupling between the chemical potential (first index) and the flux (second index). From these equations equilibrium concentrations were determined, which are the driving force behind the transport processes.

2.2.2 Optimization of the Cylindrical Case Geometry

The cylindrical configuration employed by Sundaresan and Leo lends itself well to an actuation system. Matthews et al. (2006a) subsequently sought to quantify and explore the actuation potential of nastic actuators. These studies considered the deformation and the various forces/phenomena that contributed to it. A model was created to examine the effects of changing the geometry and properties of the cylindrical model, with the intent of finding the optimum parameter set for actuation.

The model of Mathews et al. assumed an actuator construction directly analogous to that employed by Sundaresan and Leo. A plate perforated with a regular pattern of circular holes is placed along the bottom of a barrel (or cylindrical inclusion). Each one of these holes is covered with a nastic membrane. The end of the barrel is placed inside of a fluid reservoir, and the membrane actively transfers the fluid into the barrel creating nastic pressure. The top of the barrel is covered with an elastic membrane (cover plate) that deforms under the nastic pressure, creating actuation. As seen in figure 2-4, the entire assembly consists of multiple barrel-shaped inclusions placed in a surrounding material.

14
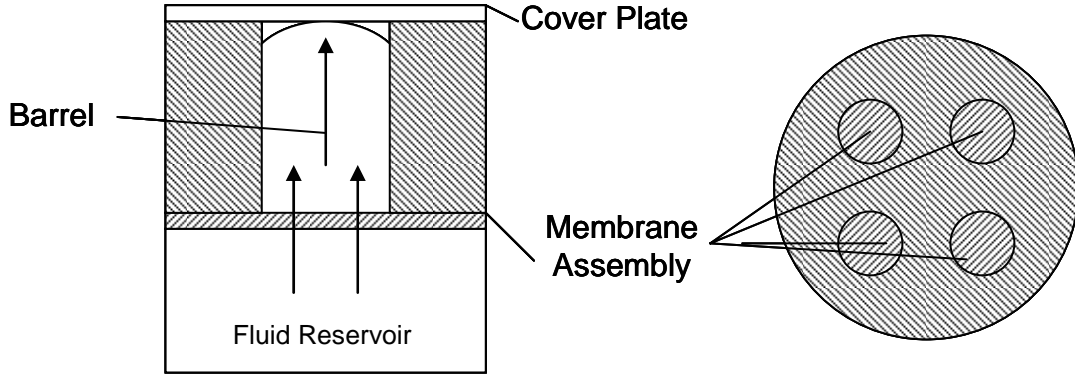
Figure 2-5 – Chemomechanical Actuator Model [Matthews, Giurgiutiu , 2006b]

The actuation deformation is divided into several parts. The total volume change is distributed across several compliance mechanisms, including the deformation of both caps ($V_{pressurecap} - V_{loadcap}$), deformation of the barrel itself (V_{barrel}), and fluid compressibility (V_{comp}).

$$\Delta V_{ISA} = \Delta V_{comp} + \Delta V_{barrel} + \Delta V_{pressurecap} - \Delta V_{loadcap} \tag{2-5}$$

From this equation, energy analysis yields:

$$p * \Delta V_{ISA} = p * \Delta V_{comp} + p * \Delta V_{barrel} + p * \Delta V_{pressurecap} + P * \Delta u_e \tag{2-6}$$

which is the internal pressure multiplied by the distance traveled. P•u_e is the incremental external work, and the rest is incremental energy expended for the compliance. The model goes on to populate each term for this equation through consideration of material properties such as bulk modulus, system dimensions, and external loading. These equations are then solved and summed to determine the total volumetric displacement. The results from these equations were then used to determine the optimum dimensions of the model (diameter, height, etc).

While useful for a narrow class of actuator optimization, the modeling strategy is not capable of projecting transient response. Because nastic motions are strongly rate dependent this seriously limits the models ability to explore novel configurations.

15

2.3 FURTHER ADAPTATIONS AND TRANSPORT MODELING

While the efforts discussed above establish proof of concept and offer the beginnings for system optimization strategies, a better understanding of the fundamental mechanisms is required. This understanding will establish the possibilities and limitations of the nastic actuator concept. In addition, while the cylindrical configuration is a convenient starting point for these developments, spherical systems such as those found in nature are expected to display superior performance. The following offers discussion of the active response of each nastic component: including each transport protein type as well as the membrane. These mathematically described mechanisms will ultimately be utilized in a model which forms the basis of this thesis work.

2.3.1 Membrane Potential

As illustrated in Figure 2-2 the membrane supports the active transport proteins as well as phase separates interior and exterior regions. When the transporters are active and the electrochemical state of these regions differ a potential difference v between the interior (subscript i) and exterior (subscript e) of the membrane exists,

$$v = v_i - v_e \tag{2-7}$$

This potential can be approximated through the Hodgkin-Huxley model (Hodgkin, Huxley, and Katz, 1952; Hodgkin and Huxley, 1952). This assumes the membrane is isopotential with evenly distributed transporters across its surface. The number of transporters is assumed large enough that overall behavior of the individual gating events averages out and that each one of the channels do not interact locally. This means that the transporters actions and influence on the surroundings do not affect their immediate neighbors – ie a pump breaking down ATP will not affect the local ATP concentration and the neighboring proton pumps will not be affected.

The capacitance of the membrane is charged by ion flux and the establishment of a diffuse double layer at each of the membrane faces (Cevc, G, 1990).

Each type of ion that permeates the membrane is represented by a resistor plus potential sources series connecting the intra and extra-cellular spaces (Figure 2-6). The resistance through the circuit is determined by the instantaneous effective permeability of the membrane which includes the effects of the channels, pumps, exchangers, and cotransporters.   The current is supplied by the transport across each of the transport proteins, which are activated by changes in concentrations and charge across the membrane
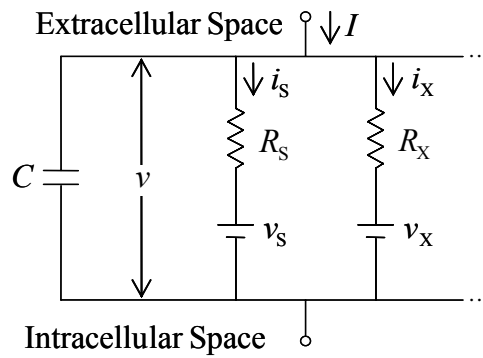
Figure 2-6 - The Membrane as a Capacitance Circuit

Using conservation of current principles, the current at the intracellular node (I) from the pH imbalance is determined to be:

$$I = C\frac{dv}{dt} + \sum i \qquad (2\text{-}8)$$

where C is the membrane capacitance and is a measurable material property. The capacitance of most biological membranes is around 1 uF/cm^2, and ranges from 0.3 and 1.5 uF/cm^2 for the black lipid membranes used in these studies. The actual value is dependent on the presence of

organic solvent in the phospholipid tails. (Ries, Choi, Blunck, Nezanilla, et al. 2004). From equation 2-8, the membrane potential with respect to time may be determined by:

$$\frac{dv}{dt} = -\frac{1}{C}\sum i \qquad (2\text{-}9)$$

2.3.2 Membrane Electrodiffusion:

In addition to having a capacitive property, the membranes are subject to passive permeability to small ions. To account for this permeation, the Nernst-Planck equation (1D) may be employed. The Nernst Planck equation determines the sum of the flux due to drift and diffusion along a concentration gradient. In one dimension form (linear), the flux for an ion S is

$$J_s = -u_s c_s \left[RT \frac{d \ln c_s}{dx} + z_s F \frac{d\phi}{dx} \right] \qquad (2\text{-}10)$$

where u_s is the mobility of ion S, c_s is the concentration of ion S and is a function of the distance x through the membrane thickness, R is the ideal gas constant, T is the absolute temperature, z_s is the valence charge of ion S F is Faraday's constant, and φ is the electric potential. (Schultz, 1980; Disalvo, Tien, 1989,) This theory of ion flux is commonly used in modeling ion channels and electrodiffusion.

This equation assumes that there is no convective flow, and that the flow is not affected by any other forces or flows. Because determining the flow experimentally is extremely difficult, the flow form is assumed to be based on an assumption about the membrane material such as homogeneity. Therefore, the electric field and gradient of electric potential is assumed to be constant across the membrane. In addition, the species concentration at the intra and extra cellular surfaces is assumed to be a linear function of the species concentration in their corresponding mediums. The linear coefficients (B_s) are assumed to be independent of the

species concentration. With these assumptions, the Nernst-Planck equation may be integrated with respect to x to yield (Bonting de Pont, 1981,)

$$J_s = -\frac{\beta_s u_s F v}{\delta} \left[\frac{[S]_i - [S]_e \exp\left(-\frac{z_s F v}{RT}\right)}{1 - \exp\left(-\frac{z_s F v}{RT}\right)} \right]$$

(2-11)

where $v = \varphi(x) - \varphi(0)$ is the membrane potential. This equation is also known as the Goldman-Hodgkin-Katz equation. A separate form of the GHK equation is required for each permeable species in the system.

When the definition of electrochemical potential (Stein, 1986) is substituted into the one dimensional Nernst Planck equation (2-10)

$$\mu_s = \left(\frac{\partial G}{\partial n_s}\right)_{\substack{T,p,n_B \\ B \neq S}} = \mu_s^0 + RT \ln[S] + z_s F v + \overline{V}sp + m_s gh$$

(2-12)

where G is the Gibbs free energy of the system. n_B is the amount of substance B in the system, μ_s^0 is the electrochemical potential at standard rate, R is the ideal gas constant, T is the absolute temperature, [S] is the concentration of species S, z_s is the valence charge of species S, F is Faraday's constant, v is the electric potential difference across the boundary of the system, Vs is the partial molal volume of S, p is the pressure difference across the boundary of the system, ms is the molar mass of species S, g is the local gravitational acceleration, and h is the height above sea level, the resulting current ignoring gravitational effects integrated across the membrane thickness is:

$$i_{diff} = z_s FAJ_S = -PA \frac{z_s F(z_s F v + \overline{V}sp)}{RT} \left[\frac{[S]_i - [S]_e \exp\left(-\frac{z_s F v + \overline{V}sp}{RT}\right)}{1 - \exp\left(-\frac{z_s F v + \overline{V}sp}{RT}\right)} \right]$$

(2-13)

where A is the area over which the diffusion is occurring, v is the membrane potential, and Ps is the permeability coefficient defined as the partition coefficient divided by the membrane thickness and multipled by the diffusion constant for the ion.

2.3.3 Biological Transporters – Introduction:

The primary categories of biological transporters considered in this study are ion pumps, ion channels, and ion exchangers/cotransporters (Figure 2-7).

An ion pump is an active transporter that uses ATP (adenosine triphosphate) to move selected ions against their electrochemical gradients. During this process the ATP is hydrolyzed, releasing energy to activate the pumps resulting in ADP (adenosine triphosphate) and P_{io} (inorganic phosphate), the concentrations of which have no impact on membrane performance. Ion pumps may move multiple types of ions in or out of the cell in a single cycle.

Channels are passive transport structures that selectively allow certain ions to travel down their electrochemical gradients. These channels alternate between gated and open, and may not always be permeable to ions. They may be activated by the membrane potential, stress in the membrane, or concentration gradients.

The exchangers and cotransporters are secondary active transporters that use the energy from the downhill movement of one species to move another species against its electrochemical gradients. The cotransporters considered in this study are simultaneous transporters, which require both species being moved to bond before they may cross the membrane. Exchangers swap ions, while cotransporters move both ions in the same direction.
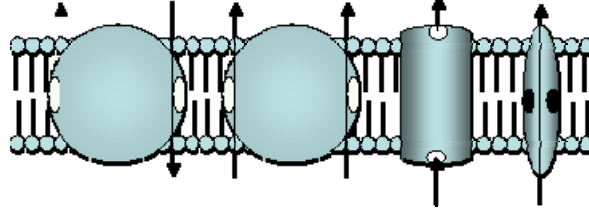
Figure 2-7 – Left to Right, Exchangers, Cotransporters, Pumps, and Channels in a bilayer membrane.

Following is a detailed discussion of each of these transport proteins.

2.3.3.1 Ion Pumps

Each of the biological components may be modeled through determining the chemical reaction rate of the component. For ion pumps the reaction may be modeled through available ATP free energy, membrane potential, and the equilibrium potentials of the transported ions. The reaction occurring at the pumps is given by,

$$ATP + mS_i^{z_x} + nX_e^{z_x} \xleftrightarrow[\beta-\alpha]{} ADP + P_{io} + mS_e^{z_s} + nX_i^{z_x} \tag{2-14}$$
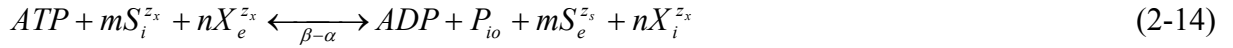
where m S ions are moved out of the cell and n X ions are moved into the cell in a single cycle. From this, the net current is given by (Endresen 2000)

$$i_{pump} = k_{pump} \tanh\left(\frac{e[(-nz_X)v + nz_X v_X] - \Delta G_{ATP}}{2kT}\right) \tag{2-15}$$

$$k_{pump} = (-nz_X)Me\lambda$$

where k_{pump} is a measure of the maximum pump current in cycles/sec, e is the electron charge, v is the membrane potential, z_X is the valence charge of ion X, v_X is the Nernst equilibrium potential for ion X, k is Boltzmann's constant, T is the absolute temperature, M is the number of pumps, λ is the net pump rate (cycles/sec), and ΔG_{ATP} is the free energy released by the breakdown of ATP. The above expressions assume uniform behavior of the pumps across the

21

membrane. In this study proton pumps were used where X represents the proton density, and the pump only transports one species through the membrane

2.3.3.2 Ion Channels

Ion channels are modeled per the Nernst-Planck equation, and employ stochastic methods to predict the gating process. The channel gates are assumed to randomly switch between completely open and completely closed states. The gating is influenced by concentration gradients and the overall membrane potential along with a gating mechanism for each channel. The current through these channels is determined by

$$i_s = k_s x \sinh\left(\frac{z_s e(v - v_s)}{2kT}\right)$$
(2-16)

$$k_s = 2z_s e u_s kT \sqrt{[S]_e [S]_i} \frac{A_p}{\varepsilon d}$$

In these equations, $x = x(t)$ is the probability of the channel remaining open. Z_s is the valence charge of the ion S, e is the charge of an individual electron, v is the potential determined by equation 2-17, k is Boltzmann's constant, T is the absolute temperature, u_s is the ion mobility through the channel, and [S] is the concentraion of ion S inside and outside the inclusion, n_s is the number of moles of ion S in the inclusion at time t, A_p is the effective pore area of the ion channel, d is the total channel length, and e_d is the effective pore length of the ion channel where 0<e<1.

The equations used assume that the area is a constant value of A_o except for a short narrow pore in the middle with an area A_p significantly smaller than the channel area. The electric field is also assumed to be constant everywhere inside the channel, and that the current is uniform through the cross sections.

22

The Nernst equalibirum potential which represents the required membrane potential for the flux of a given ion S to be zero is:

$$v_s = \frac{kT}{z_s e} \ln \frac{[S]_e}{[S]_i}$$
(2-17)

The probability of a channel being open is determined by solving the differential equation for x(t),

$$\frac{dx}{dt} = \frac{1}{\tau_s \cosh\left(\frac{2e(v-v_x)}{kT}\right)}\left\{\frac{1}{2}\left[1 + \tanh\left(\frac{2e(v-v_x)}{kT}\right)\right] - x\right\}$$
(2-18)

where t_s is the ion channel relaxation time, which is the amount of time required for channel transition between the open and closed state. This probability is dependent on both the concentrations and temperature of the system, however temperature will be held constant throughout the simulation. For this equation, the energy difference between the two states must be a function of the gating charge q and the difference in energy for both states.

$$\Delta G = q(v_x - v)$$
(2-19)

2.3.3.3 H$^+$/Sucrose Cotransporters

In the model study, a specific cotransporter was considered, namely the SUT4 H+/Sucrose Cotransporter. The reaction for the SUT4 cotransporters used in this study allows for the cotransport of H+, Sucrose, and water. The reaction is:

$$H_r^+ + Suc_e + n_w H_2 O \underset{a-\beta}{\longleftrightarrow} H_i^+ + Suc_i + n_W H_2 O_i$$
(2-20)
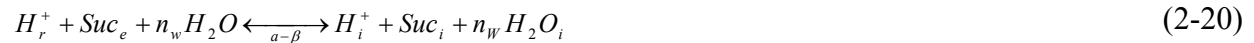
Through relating the forward and backwards reaction rates (α and β) to the energy balance from Mullins, Endresen's methodology demonstrates that the current through the cotransporter may be given by:

$$i_{\text{cotransporter}} = k_{\text{cotransporter}} \sinh\left(\frac{e\left(v - v_{\text{H}} - v_{\text{Suc}} - n_W v_{\text{H}_2\text{O}}\right)}{2kT}\right)$$

(2-21)

$$k_{\text{cotransporter}} = 2Ne\lambda\sqrt{\left[\text{H}^+\right]_e\left[\text{H}^+\right]_i\left[\text{Suc}\right]_e\left[\text{Suc}\right]_i\left[\text{H}_2\text{O}\right]_e^{n_W}\left[\text{H}_2\text{O}\right]_i^{n_W}}$$

The subscripts 'e' and 'i' denote external and internal concentrations respectively. [H^+] represents the proton concentrations, [Suc] represents the sucrose concentrations, N is the number of cotransporters, $\lambda = \alpha + \beta$ is the sum of the forward and backward reaction rates, and v_{Suc} and $v_{\text{H}_2\text{O}}$ are the sucrose and water potentials respectively, and they are used to simplify the equations.

$$v_{\text{Suc}} = \frac{kT}{e}\ln\frac{\left[\text{Suc}\right]_e}{\left[\text{Suc}\right]_i} \qquad v_{\text{H}_2\text{O}} = \frac{\overline{V}_{\text{H}_2\text{O}}}{\text{F}}\sum\pi_{\text{S}}$$

(2-22)

In the expressions for the sucrose and water potentials, $\overline{V}_{\text{H}_2\text{O}}$ is the partial molal volume of the water, $\sum\pi_{\text{S}}$ is the total osmotic pressure across the membrane, and F is the Faraday constant. Both the sucrose and the water are neutral and thus the potentials have no physical significance. All of these equations assume a rigid stoichiometry between the transported ions, and that either ion can activate the transporter.

SUT4 cotransporters were chosen for this study because experimental data collected by the experimental nastic team demonstrated that water can pass through the SUT4 components (Sundaresan, 2005).

2.3.3.4 Previous Mechanistic Nastic Model

The need to understand the basic mechanisms of nastic actuation has previously been recognized (Homison and Weiland 2005 & 2006, and Sundaresan et al. 2007). The modeling construct employed utilized the equations 2-7 through 2-20 from the previous discussion. But in order to capture the response of an engineered nastic actuator the coupling to the actuator system

was also required. A finite element methodology employing ABAQUS was employed for this purpose. The constraint of the surrounding actuator materials (for instance the cylindrical barrel) was captured via the the Mooney-Rivlin strain energy potential (ABAQUS, 2004).

$$U = C_{10}\left(\bar{\lambda}_1^2 + \bar{\lambda}_2^2 + \bar{\lambda}_3^2 - 3\right) + C_{01}\left(\bar{\lambda}_1^{-2} + \bar{\lambda}_2^{-2} + \bar{\lambda}_3^{-2} - 3\right) + \frac{1}{D_1}\left(J_{el} - 1\right)^2 \qquad (2\text{-}23)$$

where U is defined as the strain energy potential of the system where C_{10}, C_{01}, D_1 are material properties, J_{el} is the elastic volume ratio, and λ represents deviatoric stretch in the principal directions. For these studies C_{10} and C_{01} were set to values appropriate to a stiff polymer undergoing equibiaxial loading: 89.0 and 0.0 MPa, respectively. Further, the material is treated as nearly incompressible with D_1 set to 9.23E-4 MPa. Because thermal effects are ignored in this analysis, each of these values is treated as a constant. In addition, yielding is not considered in this analysis.

The final output of the model combined ion and solvent flows determine the total solvent flux through the membrane. The solvent flux is a combination of osmotic diffusion and stoichiometric active transport (Su et al 2002).

$$\frac{dV}{dt} = \overbrace{KA\left(\sum \sigma_S \pi_S - p\right)}^{\text{osmotic diffusion}} + \overbrace{\sum \overline{V}_S \frac{d}{dt}(n_S)_i}^{\text{active transport}} \qquad (2\text{-}24)$$

where K is the permeability of the membrane and A is the surface area over which flux occurs. σ_s represents the osmotic reflection coefficient and π_s is the osmotic pressure of species S. P is the hydrostatic pressure difference generated by ABAQUS. V is the partial molal volume of species S, and $d/dt(n_s)$ is given by:

$$\frac{d}{dt}(n_S)_i = \frac{\left(-mz_S i_{pump}/(mz_S - nz_X) + az_S i_{exchanger}/(bz_X - az_S) + i_{cotransporter} - i_S - i_{diff}\right)}{z_S F} \qquad (2\text{-}25)$$

which is a combination of all of the flows in the system. Lastly, osmotic pressure in a non-ideal solution is given by (Robinson; 1965):

$$\pi_S = \frac{RT}{\overline{V}_A} \frac{v_S W_A}{1000} \left((m_S \phi_S)_i - (m_S \phi_S)_e \right)$$

(2-26)

where R is the ideal gas constant, T is the absolute temperature, V_a is the partial molal volume of the solution, W_a is the molecular weight of the solution, and $m_s\phi_s$ is the molal concentration of the solution multiplied by an experimentally determined osmotic coefficient. As before, i and e denote the intracellular and extracellular spaces respectively.

The models of Homison and Weiland were calibrated with one data set from the Sundaresan and Leo experimental studies, and then used to successfully predict two other data sets. Once calibrated and validated the model was used to project the transient response to assess the ultimate possibilities for the cylindrical actuator. It was determined that large stress (~20 MPa) and fast response (less than one second) is achievable, albeit experimentally challenging.

In addition, while Homison and Weiland focused largely on the cylindrical actuator case, the modeling construct is versatile. (It should be noted that Homison performed preliminary studies of a spherical actuator case but met with only qualified success.)

With this system of differential equations approximating the behavior of the biological components embedded in the membrane, it is now possible to optimize and expand the Homison-Weiland model to other situations. The final equation (2-22) represents the expansion of an inclusion (of any geometry) as a combination of osmotic diffusion and active transport.

$$\frac{dV}{dt} = \overbrace{KA\left(\sum \sigma_S \pi_S - p\right)}^{\text{osmotic diffusion}} + \overbrace{\sum \overline{V}_S \frac{d}{dt}(n_S)_i}^{\text{active transport}}$$

(2-24)

The first term on the right hand side is largely dependent on the properties of the surrounding polymer and membrane. This term is influenced by the permeability of the membrane, its surface area, and the difference between the pressure generated through osmotic diffusion and the pressure generated by the deformation of the surrounding material.

The second term is a summation of all of the active transport mechanisms modeled in the previous section. These rapid active transports provide the initial burst of deformation, and drive the process until equilibrium concentrations on either side of the membrane are satisfied.

Because of the novel behavior of this engineered active material, several possible applications may be considered. One of the most compelling from an engineering materials perspective is development of arrays of spherical inclusions (fig 2-3). However, before attempting the cost and time intensive hurdles of experimental development, a computational study of the system's potential is warranted.

Chapters 3 and 4 of this thesis discuss the modeling methodology and subsequent results for a single, embedded spherical inclusion. In addition however, the modeling construct is inherently amenable to in-vitro studies. Chapter 5 offers preliminary consideration of the application of this modeling approach toward advancing pharmaceutical effectiveness.

3.0   MODELING METHODOLOGY

In nature Nastic movement is achieved by the controlled transport of fluid and charge across a permeable membrane. Through this accumulation of fluid, bulk deformation is achieved as the inclusion is forced to expand as it takes on water. If these inclusions are present in a large array, they may individually expand to different levels to achieve tailorable bulk deformation. However, a detailed understanding of the transient response of a single inclusion is prerequisite to projecting the response of an array. The studies to date have focused on cylindrical inclusions, while spherical inclusions are closer to that found in nature. While Homison does consider this, the investigation is limited. This thesis addresses these limitations via detailed consideration of the impact of:

1. inclusion geometry;

2. impedance matched work; and

3. varied chemical stimulus (as opposed to a step function).

This chapter reviews the modeling methodology employed to address these hurdles; Chapter 4 presents and discusses the subsequent predictions.

3.1 CURRENT MODEL

As discussed previously, experimental research has focused primarily on a cylindrical inclusion. This thesis focuses on a spherical inclusion akin to those found in nature. These

spherical inclusions are difficult to achieve in an experimental setting, so a user-defined UFLUID program operating with the finite element package ABAQUS is used to model these nastic deformations. In the simulations, only pumps and cotransporters were modeled in the membrane. This is consistent with the experimental configuration of Sundaresan and Leo. However, it is worth noting that the model is capable of projecting response for a multitude of other transporter combinations as well. As seen in Figure 3-1a, the nastic model has the ability to compute flows and behavior of four biological components: pumps, cotransporters, exchangers, and channels. Each one of these components is embedded inside the membrane which is then approximated as a capacitance circuit through the Hodgkin-Huxley equations.
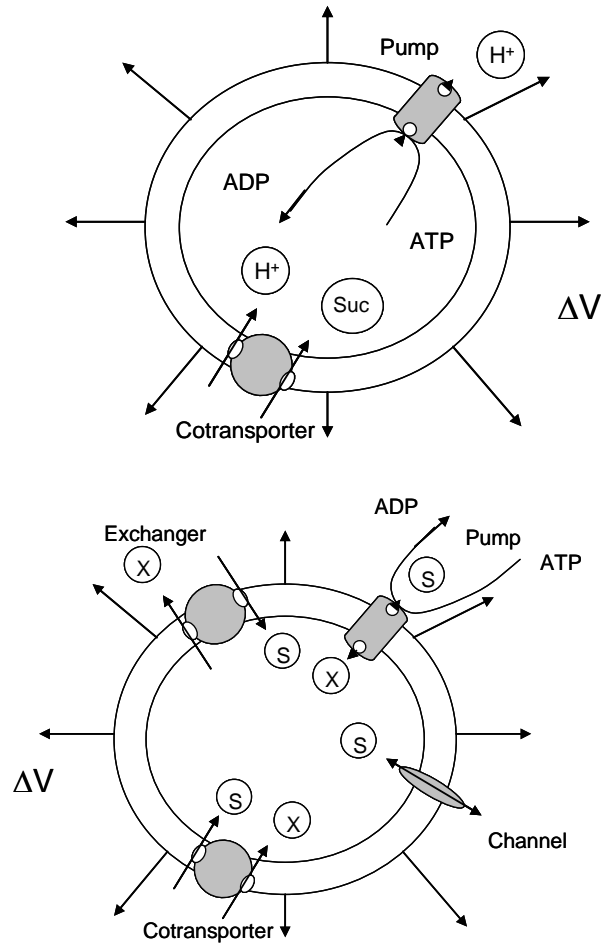
Figure 3-1a-b – Model Specific Transporter Components and General Transport Components with concentrations of S and X on either side of the membrane.

Equations for each of these components illustrated in Figure 3-1 are then used to represent current flow across the membrane. This stiff system of differential equations is then solved through the UFLUID program.

In order to predict the effect of coupling an active bilayer membrane (BLM) with an engineered inclusion, the commercial finite element package ABAQUS Standard is employed. The polymer matrix is meshed using hybrid linear 3D tetrahedral continuum elements with the hyperelastic option (C3D4H); the meshed system is illustrated in Figure 3-2. The model is

30

mirrored along all the axes to produce a full spherical inclusion, and a node is generated at the middle of the inclusion. This center node is then constricted and serves as the center for expansion. Once this model is created hydrostatic fluid elements are generated along the interior of the inclusion through modifications to the input file. ABAQUS Standard then uses implicit integration methods to expand the inclusion along a set volume range and determines the pressure generated by the polymer deformation. This Pressure-Volume information is then used to simulate pressure feedback with the UFLUID code.
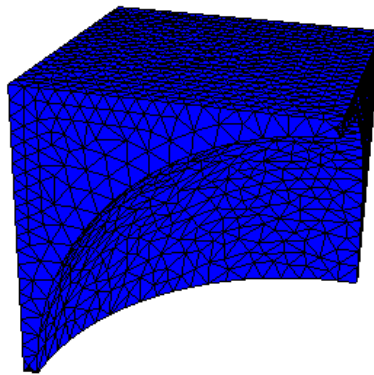
Figure 3-2 – ABAQUS Mesh Used in Modeling

Custom hydrostatic elements are created along the inner surface of the inclusion to simulate the expansion of the inclusion. Using an external UFLUID code, the inclusion is then expanded in ABAQUS from a specified initial volume to the maximum volume reached during the simulations while recording the internal pressure generated from the deformation to determine the surrounding polymers resistance to deformation (see figure 3-4 for a collection of these plots for varying geometries). These points are then plotted and a sixth order polynomial is constructed from them in Mathematica which may be used to describe the resistance to deformation provided by the surrounding polymer. This polynomial is used in UFLUID to

simulate the expansion of the polymer and provide the hydrostatic pressure difference p to determine the total change in volume per time step of the inclusion, or

$$\frac{dV}{dt} = \overbrace{KA\left(\sum \sigma_s \pi_s - p\right)}^{\text{osmotic diffusion}} + \overbrace{\sum \overline{V}_s \frac{d}{dt}(n_s)_i}^{\text{active transport}}$$ (3-1)

This equation effectively couples the hyperelastic and transport models together in the UFLUID program. This in turn provides predictions for the model based on a series of user generated inputs. This methodology allows for considerable customization and alterations for a variety of different applications. Further, it could be argued that the advantage of using ABAQUS for this modeling construct has more to do with its ability to impose a user-defined subroutine that solves a complex system of simultaneous equations than the finite element functionality which contributes only one term (p) to the predicted response. The user-defined program uses DVODE and DOPRI5 methods to solve the stiff matrix of simultaneous equations. Input files govern the properties of the inclusion, and allow the user to control the time limitations of the simulation without modifying the core program itself. This gives the program a degree of flexibility. Following is a review of the governing equations of the active components of a nastic system as employed in the model.

Membrane Potential

$$\frac{dv}{dt} = -\frac{1}{C}\sum i$$ (3-2)

Ion Diffusion

$$i_{diff} = z_s FAJ_S = -PA\frac{z_s F(z_s Fv + \overline{V}sp)}{RT}\left[\frac{[S]_i - [S]_e \exp\left(-\frac{z_s Fv + \overline{V}sp}{RT}\right)}{1 - \exp\left(-\frac{z_s Fv + \overline{V}sp}{RT}\right)}\right]$$ (3-3)

Ion Pumps:

$$i_{\text{pump}} = k_{\text{pump}} \tanh\left(\frac{e[(-nz_X)v + nz_X v_X] - \Delta G_{\text{ATP}}}{2kT}\right)$$ (3-4)

$$k_{\text{pump}} = (-nz_X)M e\lambda$$

H⁺/Sucrose Cotransporters

$$i_{\text{cotransporter}} = k_{\text{cotransporter}} \sinh\left(\frac{e(v - v_H - v_{\text{Suc}} - n_W v_{H_2O})}{2kT}\right)$$ (3-5)

$$k_{\text{cotransporter}} = 2Ne\lambda\sqrt{[H^+]_e [H^+]_i [\text{Suc}]_e [\text{Suc}]_i [H_2O]_e^{n_W} [H_2O]_i^{n_W}}$$

Strain energy potential:

$$U = C_{10}\left(\bar{\lambda}_1^2 + \bar{\lambda}_2^2 + \bar{\lambda}_3^2 - 3\right) + C_{01}\left(\bar{\lambda}_1^{-2} + \bar{\lambda}_2^{-2} + \bar{\lambda}_3^{-2} - 3\right) + \frac{1}{D_1}(J_{\text{el}} - 1)^2$$ (3-6)

Solvent Flux

$$\frac{dV}{dt} = \overbrace{KA\left(\sum \sigma_S \pi_S - p\right)}^{\text{osmotic diffusion}} + \overbrace{\sum \bar{V}_S \frac{d}{dt}(n_S)_i}^{\text{active transport}}$$ (3-7)

$$\frac{d}{dt}(n_S)_i = \frac{\left(-mz_S i_{\text{pump}}/(mz_S - nz_X) + az_S i_{\text{exchanger}}/(bz_X - az_S) + i_{\text{cotransporter}} - i_S - i_{\text{diff}}\right)}{z_S F}$$ (3-8)

$$\pi_S = \frac{RT}{\bar{V}_A} \frac{v_S W_A}{1000}\left((m_S \phi_S)_i - (m_S \phi_S)_e\right)$$ (3-9)

3.2 GEOMETRY VARIATION

The configuration considered in this work is a single spherical inclusion (or vesicle) of fixed volume embedded in a stiff polymer matrix that permits fluid flow. The geometry of the surrounding material is scaled to varying ratios of *R/L*, where *R* is the radius of the spherical

inclusion and *L* is half the length of one of the sides (Figure 3-3). The membrane is located

along the inner surface of the inclusion, and the fluid must pass through the permeable outer

polymer matrix to reach embedded transporters.
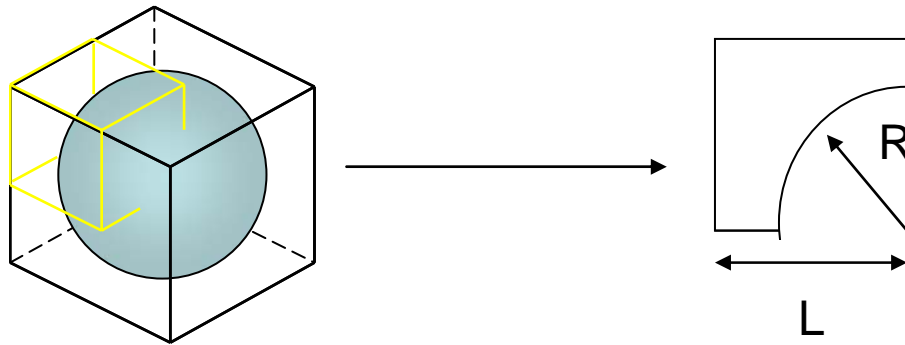
Figure 3-3 – Basic Inclusion Geometry Description

In this section the response of the embedded inclusion is considered; the following

section will consider the response of the actuator as a whole. In both analyses the response to

stimulus is considered for four geometrical configurations with *R/L* ratios of 0.60, 0.75, 0.90, and

0.95. Further, each of these cases is considered for both the "Baseline" and "Increased

Performance" initial conditions dictated by Table 1. The "Baseline" input parameters adapt the

experimentally established parameters from studies of a cylindrical inclusion where only the base

supports an active BLM (Sundaresan et al, 2007), to that of a spherical inclusion entirely

surrounded by active BLM (Freeman and Weiland, 2007). The "Increased Performance"

parameters employ values that result in optimized performance for an unmodified spherical case

(Homison, 2006). Application of these values is expected to result in improved performance for

each of the geometries considered here, however the parameters should not be considered

optimized for these geometries. Inclusion response for one of these cases (*R/L* = 0.90) is

subsequently considered for a range of membrane permeability values to determine the effect of

altering polymer properties along with geometries. In addition to altering the geometry, variation

of other system parameters such as membrane permeability and system pH are considered

Table 3-1 - Initialized System Configuration for Experimentally Established Baseline Parameters and Hypothetical Increased Performance Parameters

Parameter	Notation	Units	Baseline	Increased Performance
Int. & ext. pH	$pH_e=pH_{i0}$		5	4
Int. & ext. Sucrose conc.	$[Suc]_e=[Suc]_{i0}$	mM	1.0	5.0
Net Cotrans. Current per transported species*	$N_{SUT4}e\lambda_{SUT4} \cdot ([W]^{ne}_w[W]^{nw}_i)^{1/2}$	pA/(mM H$^+$)· (mM Suc)	65	650
Cotransporter H_2O Stiochiometry	n_w		350	700
Membrane Capacitance	C	μF	0.105	0.105
Membrane Permeability	K	x10^{-15} m^3/Ns	1.65	1.65
Membrane Surface Area	A	x10^{-2} (μm)^2	1.57	1.57
Osmotic Reflection	σ		1	1
Max. Ion Pump Current	k_{pump}	pA	65	65
Energy release from ATP hydrolysis	ΔG_{ATP}	x10^{-20} J	-1.0	-1.5
Membrane Potential	v_o	V	0.0	0.0
Inclusion Volume	V_o	x10^{-4} (μm^3)	5.18	5.18

*There is insufficient experimental data to isolate a maximum cotransporter current; alternatively

the lumped value summed over all system cotransporters with respect to transported species can

be inferred from experimental data.

3.3 PRESSURE-VOLUME CALIBRATION CURVES

Based on any arbitrary stimulus that results in increased inclusion pressure, the elastic response of the surrounding polymer will constrain the final inclusion volume. This response is dependent only on geometry and polymer mechanical properties. In this analysis properties consistent with a typical stiff polymer are imposed (C_{10} = 89 MPa, C_{01}= 0 in the Mooney-Rivlin Strain Energy Potential); the simplifying assumption of quasistatic material behavior is imposed. Once specific polymer candidates are identified it will become appropriate to also consider the dynamic response of that material.

The results of predicted polymer response to increased inclusion pressure are employed to calibrate the anticipated back pressure during active BLM response in the UFLUID. The results, as expected, show that increasing the inclusion volume fraction results in lower peak pressure and higher peak volume. The pressure-volume plots show linear behavior in all cases (figure 3-4).
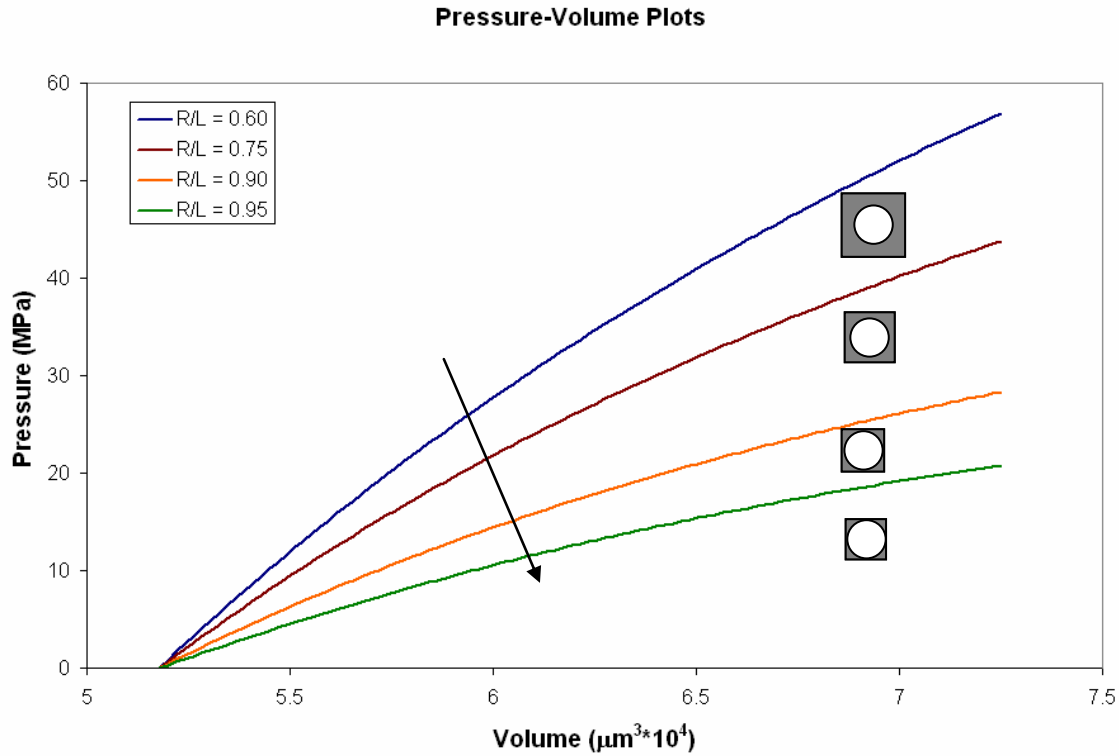
Figure 3-4 – Pressure-Volume Response for Varied R/L Ratios. The arrow indicates the trend for increasing R/L ratio.

3.4 BLOCKED FORCE CALCULATIONS

The foregoing modeling approach explores the active response of the embedded inclusion. This understanding is necessary before any assertions regarding actuator response may be made. However, the true utility of this novel active material must ultimately be considered through the expected bulk material response. The following offers a strategy for projection of the free strain, blocked stress, and impedance matched work per unit volume for this material based on the response of the single volume element (Fig. 3-5).

37

While introducing a boundary condition of zero displacement along an edge in a finite element analysis is straight forward, the resultant load at each point along that constrained surface varies with position. In application, an array of these volume elements would experience a blocking force akin to having placed a rigid plate across the blocked surfaces, where the value of interest is the total force required to prevent the displacement of the rigid plate. Quite a number of approaches are available to generate this parameter, with varying degrees of complexity and accuracy; here a rather simple application of thin shelled pressure vessels analysis is adapted for estimating the blocked force.

To implement this approach, the inclusion is approximated as a spherical pressure vessel. Balance of forces dictates that the hoop stress acting on the pressure vessel cross section must balance the internal pressure, resulting in the classic derivation, $\sigma_\theta = pr/2t$, where p is the internal pressure, r is the radius of the inclusion, and t is the thickness of the membrane. Employing the same approach in the deformed blocked stress state, where the pressure vessel is now oblate, balance of forces may be employed to infer the value of the blocked force required to sustain the blocked configuration.

The values estimated for hoop stress via this method are checked against the free displacement predictions for accuracy; the approach proves to be a reasonable approximation for the *R/L* cases of 0.75, 0.90, and 0.95. The error associated with the approximation becomes large for the case of *R/L* = 0.60 and this case will not be presented.

Because the dimensions of the model are small, the resulting blocked force values are also small. Thus to better enable direct comparison between these predictions and the behavior of other active materials blocked stress (divide by L^2) results are presented.
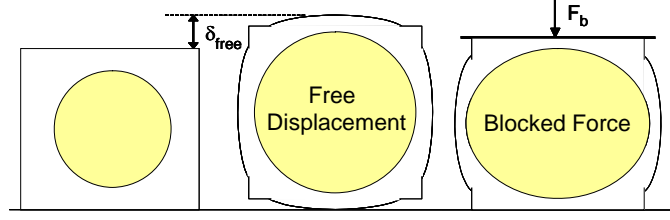
Figure 3-5 – Illustration of Free Displacement and Blocked Force

3.4.1 Free Displacement

The free displacement as illustrated in Figure 3-5 is easily determined from the finite element analysis for each case. Because of the small size of the model the parameter is presented in terms of free strain (divide by *L*) to enable comparison with other active materials. The strain is calculated through the change in radii, and while this term does not represent the strain in the surrounding polymer it does provide an appropriate term for the desired displacement.

3.4.2 Impedance Matched Work

Impedance matched work is given as

$$W = \frac{F_b \delta_{free}}{8} \tag{3-10}$$

or under the assumption of uniform material response it may be presented on a per unit volume basis as

$$w = \frac{\sigma_b \varepsilon_{free}}{8} \tag{3-11}$$

where σ_b is blocked stress and ε_{free} is the free strain/displacement from the previous section. The surrounding material is assumed to be incompressible, therefore the displacement at the outer edge will be roughly equivalent to the displacement of the inner wall of the inclusion. The expression for impedance matched work per unit volume should provide a reasonable means to

anticipate this property in the bulk material. In addition, as a means to enable better understanding of this active material, it may be instructive to also consider the work done by the inclusion. With Figure 3-6 as a reference, this value of work will be calculated as

$$w_{incl} = \frac{(p)\left(\dfrac{r_f - r_i}{r_i}\right)}{8} \tag{3-12}$$

where p is the peak internal pressure attained for each case, r_i is the initial inclusion radius and r_f is the final inclusion radius.
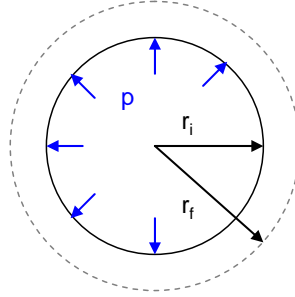
Figure 3-6 – Illustration of Inclusion Work

3.5 FUEL LIMITATIONS

In the previous studies by Homison and Weiland the existence of a constant, infinite reservoir of stimulus in the surrounding polymer is assumed. However, as each of the inclusions reacts to the external stimuli, this external stimuli will be gradually diminished. Therefore it is important to study the effects of a varying fuel source (in this case ATP) on the behavior of the system.

Assuming that the inclusions are floating close to each other in a fluid flow, as each one consumes a small amount of ATP (or fuel) from activating the ion pumps, they also consume the remaining available fuel or trigger for the entire group. The code was altered to include an algorithm for multiplying the ATP loss per timestep by a set constant representing the number of inclusions present to model this behavior.

4.0   RESULTS AND DISCUSSION

4.1 TRANSIENT RESPONSE

When considering the transient description of inclusion peak volume and peak pressure (figure 4-1), parameters of note are time to peak, time at peak, and relaxation time, which collectively represent the time of the entire transient event. Experimental validation of this modeling approach has demonstrated that the relative shapes of the transient response curves are appropriate, but it is premature to claim high levels of accuracy on the absolute time corresponding to each of these transient responses (current simulation predicts expansion time of milliseconds). Due to the initial rapid expansion of the inclusion, the plots are presented on a log scale to better illustrate the changes in expansion behavior. Detailed consideration of the total time elapsed for any aspect of response should focus on relative performance improvements rather than absolute prediction. Thus for the current state-of-the art, these sequentially occurring time zones are loosely defined.

Baseline Volume Expansion
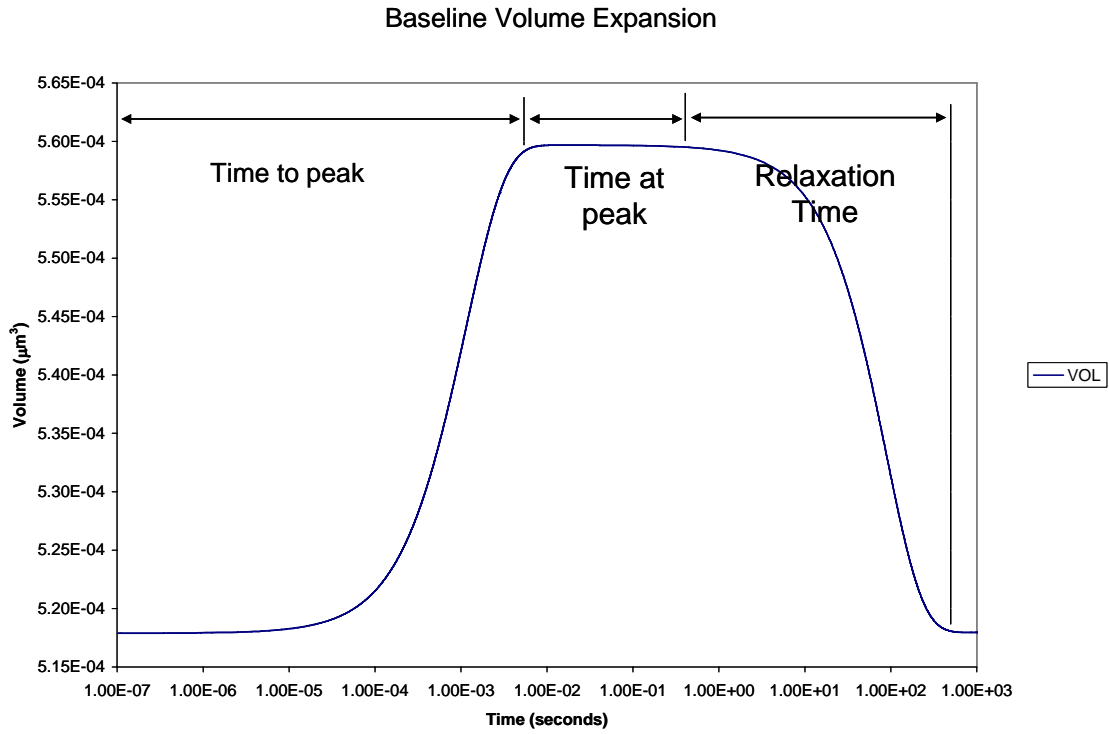
Figure 4-1 – Illustration of Transient Values.

4.2   VOLUME RESPONSE

For the initialized baseline conditions detailed in table 3-1, increased *R/L* ratios (reducing the surrounding polymer volume) results in modestly increased peak volume and time at peak (fig 4-2a). In addition, the final equilibrium volume is modestly increased for increased *R/L*. The predicted time to peak is increased slightly as the R/L ratio is increased.

For the Increased Performance input parameters (Fig. 4-2b), the peak volume response is dominated by the transport side of the reaction; the hyperelastic components have little effect. Because of this a plateau effect is observed, with time to peak significantly faster in comparison

43

to the Baseline case (~ 0.0001 *seconds*). In addition, the peak itself is significantly increased. Upon initial observation, it appears that each case reaches peak volume at about the same time. After examining the files, it is demonstrated that each simulation reaches the "plateau" at around the same time; however each model continues to expand slowly until a certain point around halfway through its plateau.
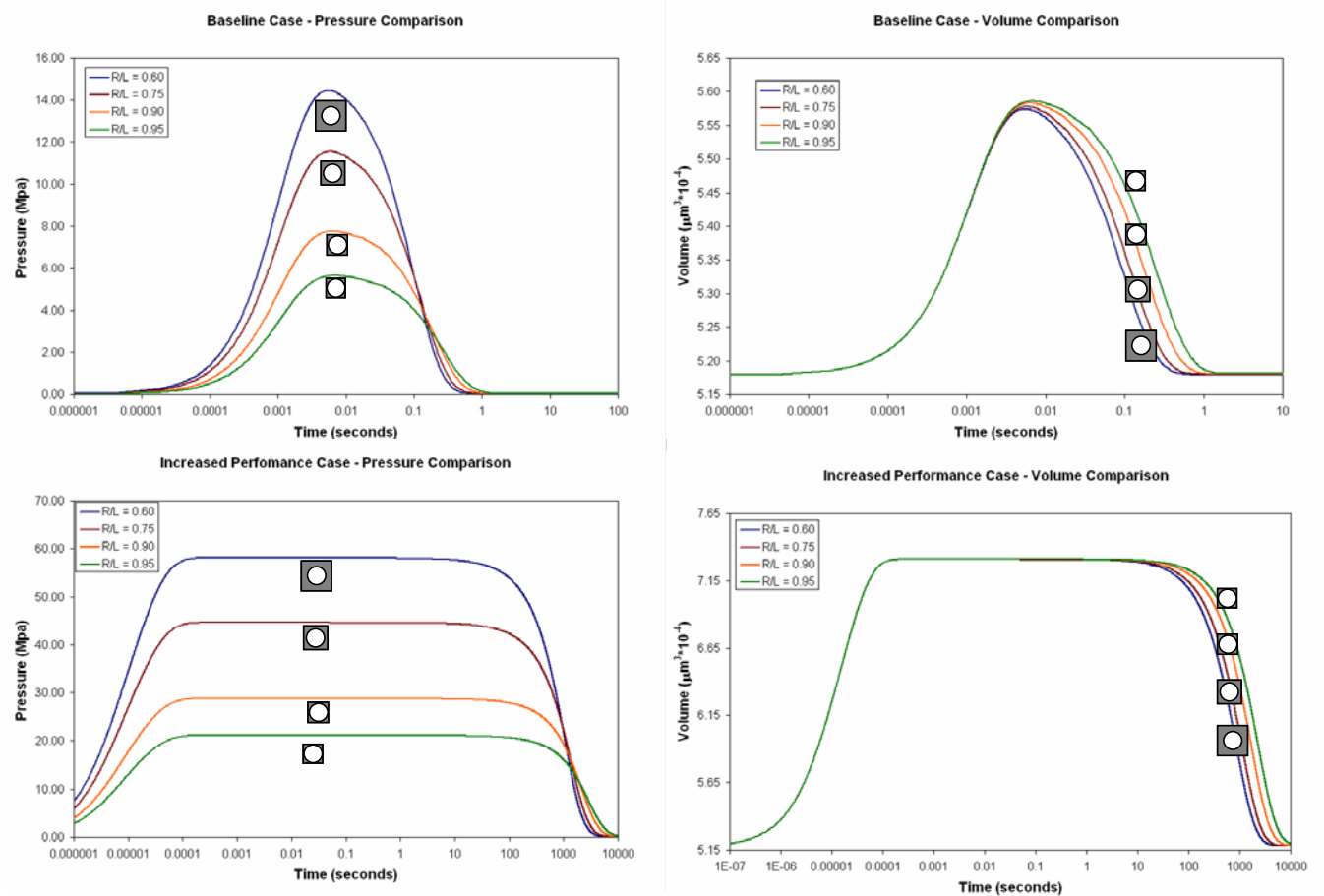

**Figure 4-2a-d (cw from top left corner) – Pressure Volume results for Baseline and Optimized Case**

4.3 PRESSURE RESPONSE

The pressure transient response is highly dependent on the geometry of the model. (Figs. 4a and 4c). Higher R/L ratios display significantly reduced peak pressure while the time to peak is modestly shorter for decreased R/L ratios.

For the Baseline input parameters the predicted peak pressure occurs at slightly different times for each case. As the surrounding material decreased, the time to peak volume continued to increase, resulting in a delayed peak pressure. The final equilibrium pressure is identical in all cases, seen at the far right end of each plot. This is the equilibrium pressure reached when the minimal pressure due to deformation still present in the matrix is balanced out by the remaining amount of osmotic pressure due to concentration changes across the membrane.

For the Increased Performance parameters, the peak pressure for each R/L case is significantly increased.   However as each simulation reaches the peak volume plateau at similar times, the peak pressure is also reached at similar times. Thus the peak pressure and volume for the High Performance case not only coexist at some moment in time, but also overlap for most of the transient event.

While the overall impact of changing the surrounding material may look minimal on a log plot, it is helpful to view the results with respect to a linear time scale (figure 4-3).
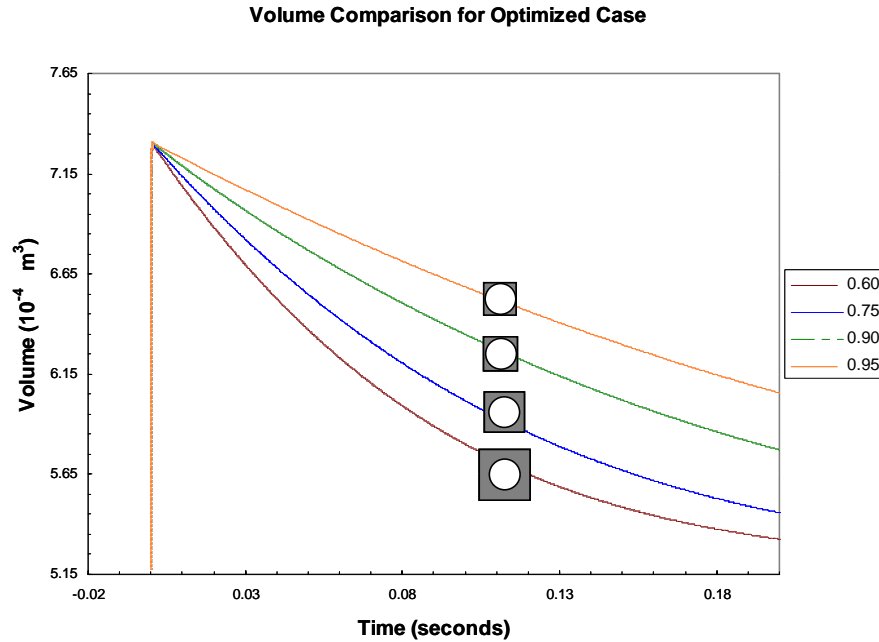
Figure 4-3 – Volume Expansion on a Linear Time Scale

From this plot it is apparent that reducing the surrounding material has minimal impact on the initial rapid expansion, however the rate at which the inclusion relaxes back towards its initial state is greatly affected. From this it may be observed that the rate of volume decrease is directly dependent on the different between the osmotic gradient pressure and the pressure generated through coupling the expansion with the surrounding material. The osmotic pressure quickly reaches a constant value, and the deformation dependent pressure will gradually decrease down to a value slightly above the osmotic constant pressure. As seen in the literature review, the gradual decrease in volume is the result of the difference between the pressure generated by deformation and the osmotic pressure. With less surrounding polymer, this results in a much lower deformation pressure which leads to a slower relaxation of the inclusion.

46

4.4 CONSIDERING PRESSURE AND VOLUME TOGETHER

The results illustrated in Figure 4-2 show that reducing the volume fraction of the surrounding polymer (increasing *R/L*) has modest if any effect on peak volume, but peak pressure is significantly influenced by geometry; lower *R/L* ratios result in increased pressure. But intuitively, reducing the ratio too far will result in negligible expansion of the actuator as a whole due to increased resistance to deformation in the polymer. Thus, akin to other active materials there remains a trade off between blocked stress and free displacement that must be identified. However, in comparing the predictions for the Baseline versus the Increased Performance response of the inclusion, it becomes clear that the total magnitude of free strain and blocked stress, as well as the time response of the peak values may be manipulated. Through this manipulation it may be possible to have an array of inclusions which will expand at specifically tailored rates in relation to each other, a possibility which will be explored further later in the thesis.

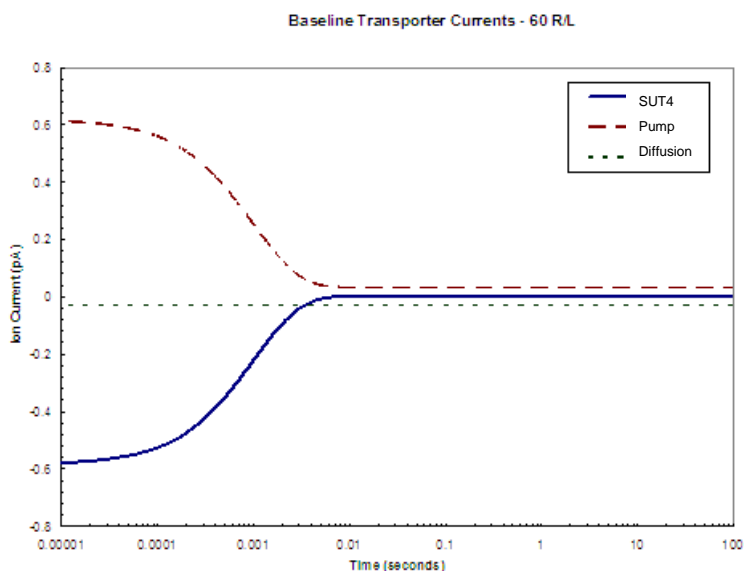## 4.5 TRANSPORTER CURRENT RESPONSE

The predicted current flows generated by the biological transporters and the flux of water across the membrane are illustrated in Figure 4-4. Due to the rapid establishment of the membrane potential, the cotransporters are able to maintain the constant pH gradient while pumping the water and sucrose into the inclusion faster than the fluid can diffuse out of the

inclusion. This constant pH gradient allows the electric currents from the pumps, diffusion, and cotransporters to cancel each other.

The currents were examined at for two extremes in *R/L* ratios: .95 and .60. After comparing the two cases, it was found that the difference between the two was minimal. While decreasing the amount of surrounding polymer volume had an impact on the pressure-volume results, no changes were observed in the current flow. The current flows operate independently of the pressure and are functions only of the concentrations on either side of the membrane.

Figure 4-4 - Baseline Transporter Currents- no observable change for differing geometries

4.6   THE ROLE OF MEMBRANE PERMEABILITY

Both the mechanical integrity and permeability of a naturally occurring BLM are insufficient for the needs of engineered active materials. However, it has been demonstrated that

the proteins responsible for active response can be introduced into an artificial membrane, which

introduces the potential for control over these basic membrane properties (Sundaresan and Leo,

2006b). The above study implicitly assumes that the mechanical integrity of the membrane

matches (or is at least supported by) that of the surrounding polymer. The role of this property is
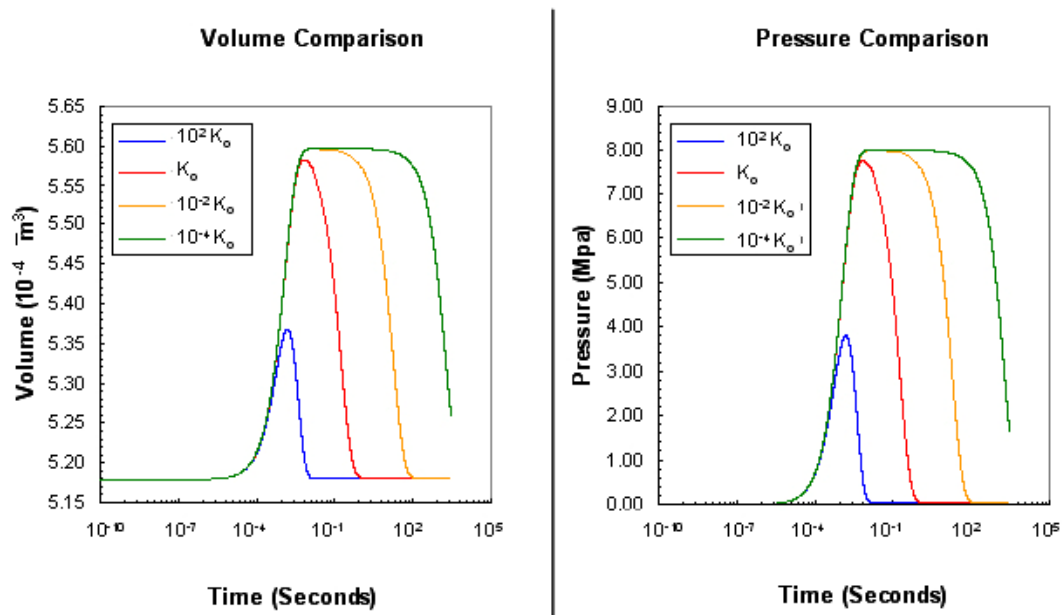
considered here.

Figure 4-5a-b – Graphs of the pressure and volume results after varying the permeability of the membrane

Previous studies of BLM permeability in a *R/L* = 0.50 Baseline case predict that the time at peak will increase as permeability decreases, but little to no change in peak values is observed. Figure 4-5 illustrates the predicted effect of varying the permeability for the case of *R/L* = 0.90 where all other properties continue to correspond with the Baseline input parameters. In this study the baseline permeability of 1.65 x 10^{-15} is varied by factors of 10^{-4}, 10^{-2}, 10^{0}, and 10^{+2}.

Figure 4-5 illustrates that increased permeability results in significant degradation of the inclusion response. However, the peaks in pressure and volume increase modestly for decreased permeability, while the time at peak is significantly increased. The time to peak continues to correspond with the Baseline rate of ~.01 seconds) for all cases. Similar trends are observed for the other geometries.

Based on these analyses, variation of BLM permeability may be used to tune the duration of the total actuation event with negligible impact on the magnitude of response.

4.7 BLOCKED FORCE RESULTS

Using the equations developed in the modeling methodology chapter, blocked force calculations were obtained for three different *R/L* ratios. The values needed for equation $\sigma_{\theta} = pr/2t$ were determined through examining the stress results along the exposed edges of the finite element model, while the radius and thickness of the inclusions were pre-determined. After gathering the data for .75, .90, and .95 *R/L* values, the results were plotted. The values for .50 and .60 *R/L* were discarded due to high amounts of error, as the stress along the shell varied too intensely due to increased shell thickness.

Figure 21 illustrates that the peak blocked pressure developed displays considerable variability with both geometry and initial system conditions. As expected, Increased Performance input parameters result in increased blocked pressure; in addition, blocked pressure increases as *R/L* increases. Consideration of decreased permeability values results in the same predicted magnitudes already presented in Figure 4-6 (only the time that they are sustained is affected).
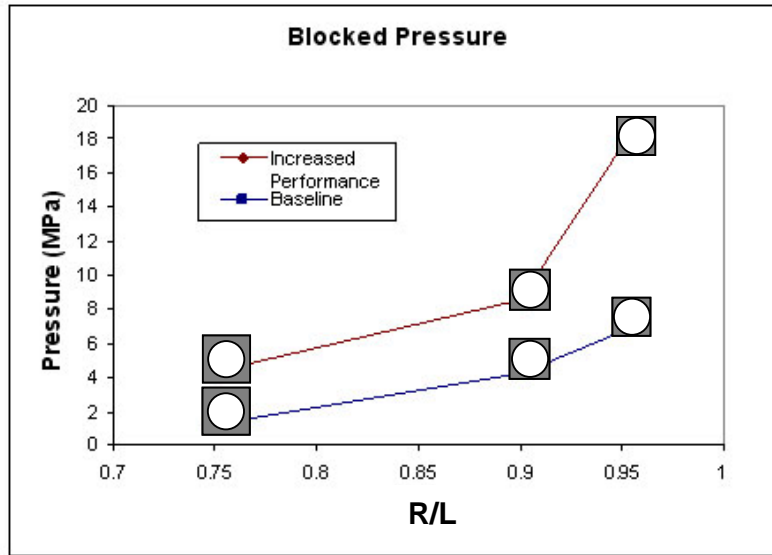
Figure 4-6 – Blocked Pressure vs. R/L.

4.8 FREE DISPLACEMENT

The free displacement as illustrated in Figure 4-7 is easily determined from the finite element analysis for each case. Because of the small size of the model the parameter is presented in terms of free strain (divide by L) to enable comparison with other active materials. Figure 4-7 illustrates that the free strain is relatively insensitive to geometry for the cases considered here.

51

As in the case of blocked pressure, decreased permeability values do not alter the magnitudes of the predicted free strain.
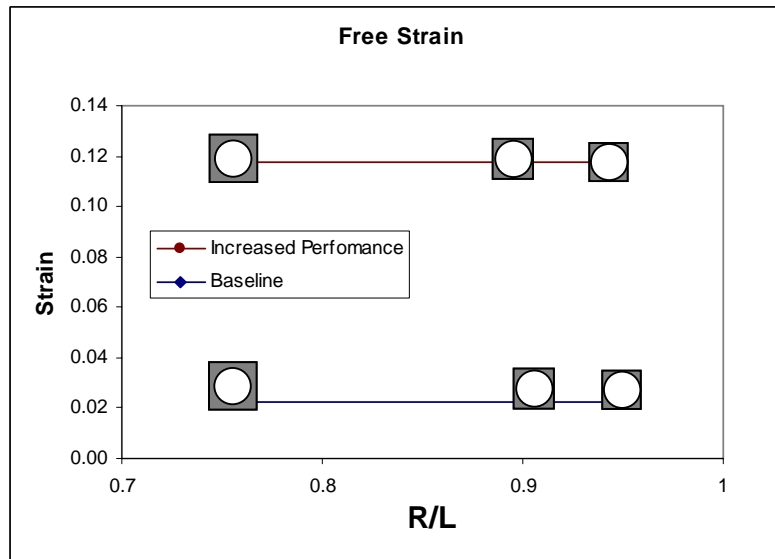
Figure 4-7 – Free Strain for fixed geometry and varied permeability

4.9 IMPEDANCE MATCHED WORK

Using the results from the free displacement and blocked force/pressure studies, it is possible to determine the total work performed at both the inner membrane and the outer surface. Using equations from the modeling methodology section on impedance matched work, impedance matched work was determined for both the increased performance and baseline case at the inclusion and to the surroundings with varying R/L ratios and differing membrane permeabilities.

Table 4-1 - Impedance Matched Work for Varied Permeability, Geometry, and Input Parameters. Area of Interest is Highlighted.

Permeability	Impedance Matched Work (kJ/m^3)				
	Increased Performance Parameters			Baseline Input Parameters	
10^{-4} K_0	Model	Inclusion		Model	Inclusion
0.75	48	712		2.6	35.9
0.9	113	480		10.8	24.7
0.95	246	359		17.8	18.3
10^{-2} K_0					
0.75	48	712		2.6	35.8
0.9	113	480		10.8	24.6
0.95	246	359		17.8	18.3
10^{0} K_0					
0.75	48	710		2.5	32.5
0.9	114	479		11	23
0.95	246	358		17	17.3
10^{2} K_0					
0.75	45	627		~0	3.9
0.9	176	437		1.5	4.2
0.95	254	334		3.8	4.2
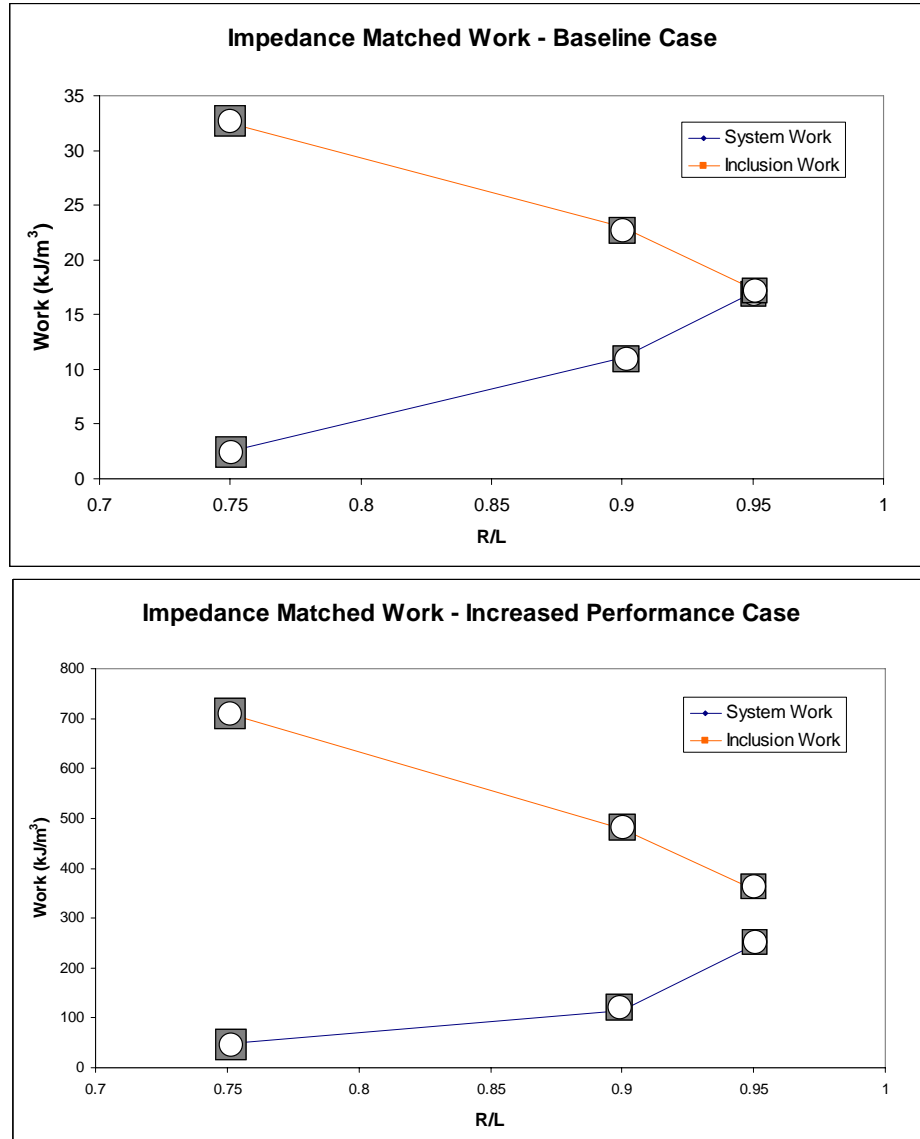
Figure 4-8a-b –Plot of the work done by the membrane (inclusion work) vs amount of work transmitted to

the surroundings (system work)

Table 4-1 summarizes the impedance matched work predictions for the inclusion alone as well as the volume element as a whole for varied permeability, geometry, and input parameters. The mechanical properties of the surrounding polymer are held fixed in this analysis; ultimately this parameter will also play in important role in material system design.

It is helpful to compare the capabilities of the Nastic inclusion to the impedance matched work generated by common actuators such as SMP (shape memory polymer) and conducting polymers. For the nastic inclusion, the maximum strain reached remained constant for each of the geometries considered around 12% (figure 4-7). The maximum blocked pressure generated reached about 18 MPa (figure 4-6). Compared to data taken for SMPs, the maximum strain is less (SMPS reach 15-50% maximum strain while Nastic reached 12%.), with a much lower blocked stress (18 MPa for Nastic compared to $10^3 - 10^4$ MPa for SMP). When compared to conducting polymers, the maximum strain is comparable (12% for Nastic compared to 9%-25% for conducting polymers) while the maximum blocked force is much higher (18 MPa for Nastic compared to .5– 1 MPa).

In the previous section it is noted that the inclusion peak pressure increases as R/L decreases; however, by intuitive arguments as R approaches zero, progressively decreasing R/L cannot be representative of the optimum work available from a nastic material. This argument is validated in the predictions of Table 3.

Consider one case of Increased Performance input parameters (shaded region in Table 4-1). As R/L decreases from 0.95 to 0.75 the work done by the inclusion nearly doubles. However, the reverse trend is observed for the volume element as a whole. If an ad hoc definition of efficiency is imposed, this suggests that the efficiency for the $R/L = 0.75$ case is ~7% while the efficiency for the R/L = 0.95 case is ~70%. These numbers for efficiency are obtained through

comparing the amount of work done at the inclusion to the amount of this work that is transmitted to the system.

In the earlier discussion of the effects of varied permeability, based exclusively on the reduced active response with increase permeability, it might have been tempting to presume increased permeability is always undesirable. However, for the High Performance input parameters, increased permeability also increases the "efficiency." Thus, it is conceivable that increased permeability may be employed to tune both the magnitude and efficiency of response in the High Performance regime. (The predictions do not suggest that the same would be true for Baseline cases.)

Similarly, it is interesting to note that the efficiency of the response for Baseline input parameters is generally higher than that of the Increased Performance parameters; in some instances the efficiency is extraordinary, with a maximum of 98%.

It should be noted that the interpretation of efficiency addressed here should be approached with caution. A more appropriate definition of efficiency will examine the chemical energy required to stimulate the system. However, in the context of this thesis, which seeks primarily to define the role of material system design, such as geometry, the mechanical-to-mechanical efficiency offers appropriate insight.

While the impedance matched work is an important parameter, the rate of response is also of significant importance in active materials applications. Because the final state of the inclusion (species concentrations, etc.) has been significantly altered from its initialized state, this study neither confirms nor dismisses the possibility of sustaining a deformed state indefinitely through some controlled feed of ATP. Similarly, this study neither confirms nor dismisses the potential for cyclic response in this novel class of materials. However, this effort does suggest that the initial

rate of response for an engineered nastic material could be extraordinarily fast (predicted at ~0.001 seconds), while the deformed state could be held for orders of magnitude longer (predicted at several minutes or more as membrane permeability approaches zero). The input here is a pulse of ATP energy. This input may also be modeled as a step function, as the amount of ATP used per cycle is not enough to cause a substantial difference between the amount of ATP available at the onset of the pulse and the amount available after the expansion.

4.10 VARIABLE STIMULUS STUDIES

In previous studies a single step function stimulus, for instance of ATP, is assumed. In application the stimulus will vary with time, for instance as the ATP is consumed its concentration will diminish. It is therefore desirable to better understand the behavior of the nastic system under varied stimulus. However, because introduction of a continuous functional of ATP availability represents a substantial computational burden the approach considered here employs the introduction of a second step function at some point prior to system equilibrium.

As illustrated in Figure 4-9, two 1-step ATP stimulus reference cases (4.12E-12 and 8.24E-12 moles) are provided. The two 2-step cases are: (1) begin with a step function of ATP free energy availability of 4.12E-12 moles followed by a decrease to 2.06E-12 moles (half of the original amount), and (2) begin with a step function of ATP free energy availability of 4.12E-12 moles followed by an increase to 8.24E-12 moles (double the original amount).
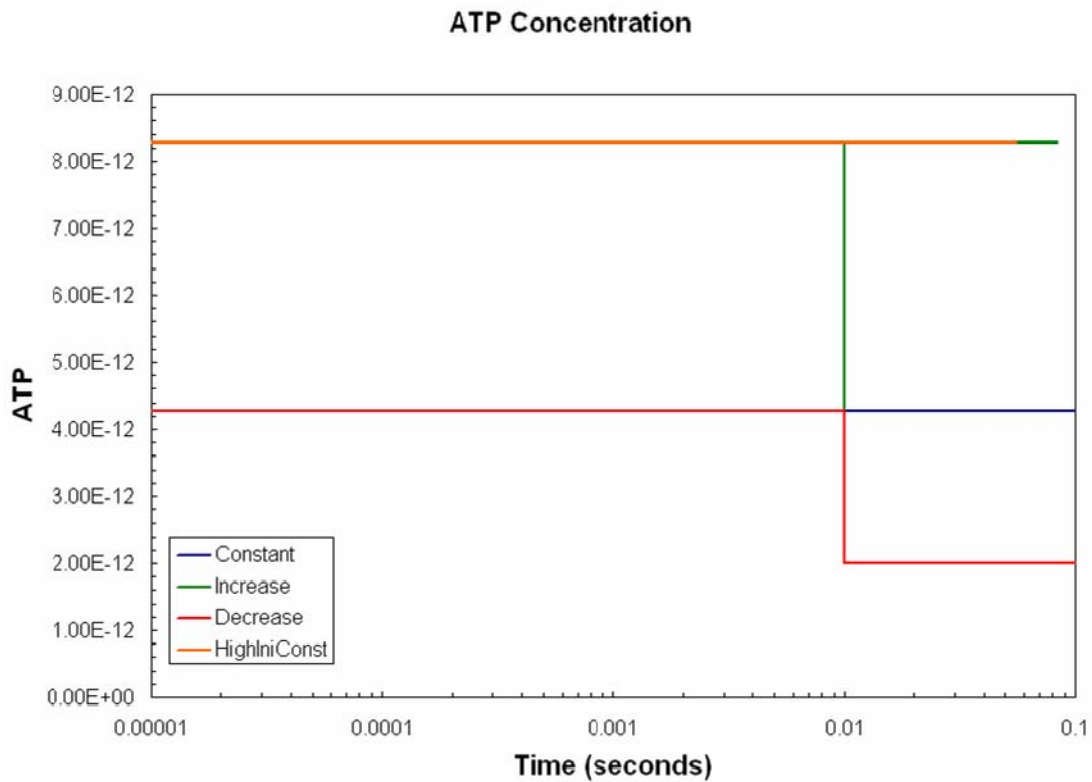
ATP Concentration

Figure 4-9 – Plot of the ATP concentrations for the simulation

The projected transient response is illustrated in Figure 4-10. The inclusion response is described via volume with respect to time for the 4 ATP stimulus cases.

As expected the reference case for a 1-step function of higher concentration ATP follows a path of similar shape but steeper ascent to equilibrium as compared to that of the baseline. Also as expected, the 2-step cases begin their path along that of the baseline case. However, upon application of the second step in stimulus, the response is unexpectedly step-like. For the case of the second step corresponding to an increase, rapid volume increase to that associated with the alternate constant stimulus is observed. While not illustrated, the decreased ATP stimulus case similarly approaches the new path. The significance of this is that once ATP activation has begun, the volume of the inclusion is projected to have high sensitivity to stimulus and therefore

58

may be controlled through the simple limitation of available fuel or stimulus instead of requiring the implementation of a complex control strategy for the system of inclusions.
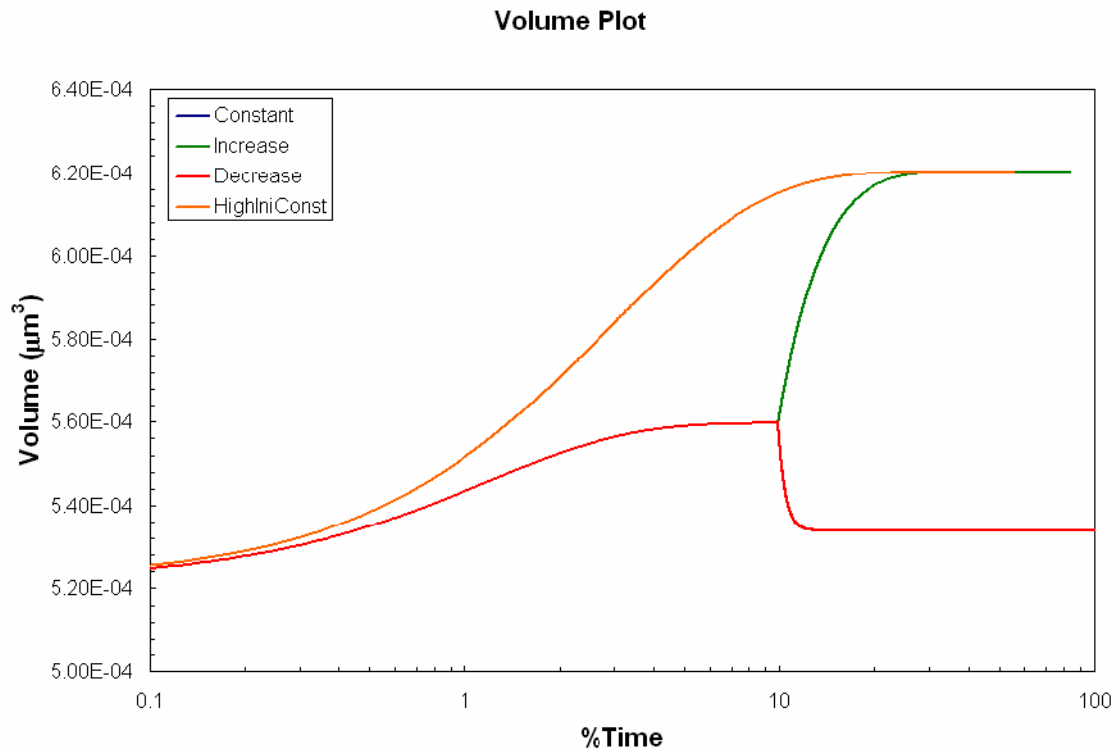
Figure 4-10 – Plot of the Volume predictions after subjecting the model to a sudden change in ATP

Because pH gradient has also previously been applied as stimulus control a similar study is provided for variation of this gradient. In this instance it is computationally viable to introduce a continuous functional. As illustrated in Figure 4-11 three cases are considered: a baseline case for constant external pH (mirroring previous studies), a case where pH is increased at a linear rate of .15*%time, and a case of rapid linear increase of .75*%time. (%Time scale is used due to discrepancies in time scale, however the trends reported by the model are accurate)
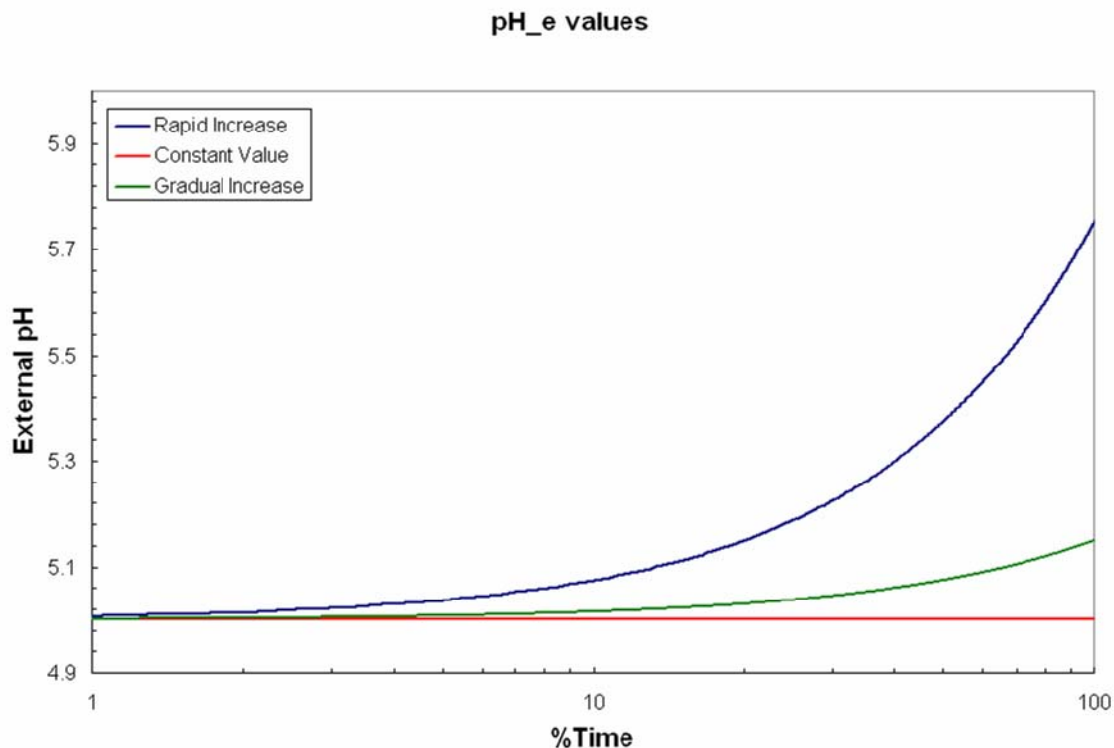
Figure 4-11 – Level of pH change for prediction

Figure 4-12 provides projected response for the 3 cases. Due to the rapid initial expansion of the inclusion, the impact of the external pH change is minimal before the inclusion reaches its peak volume. Therefore, the affect of varied pH appears after the peak volume is attained. Further, based on computational burden the projections for the 2 variable pH cases are not taken to equilibrium, but the evidence suggests that the initial expansion begins to fall off prematurely for these cases. This trend toward volume decrease with increasing external pH may warrant further study.

The following chapter offers a discussion of potential in vitro applications for this modeling methodology. The observed pH response may become especially important in this application.
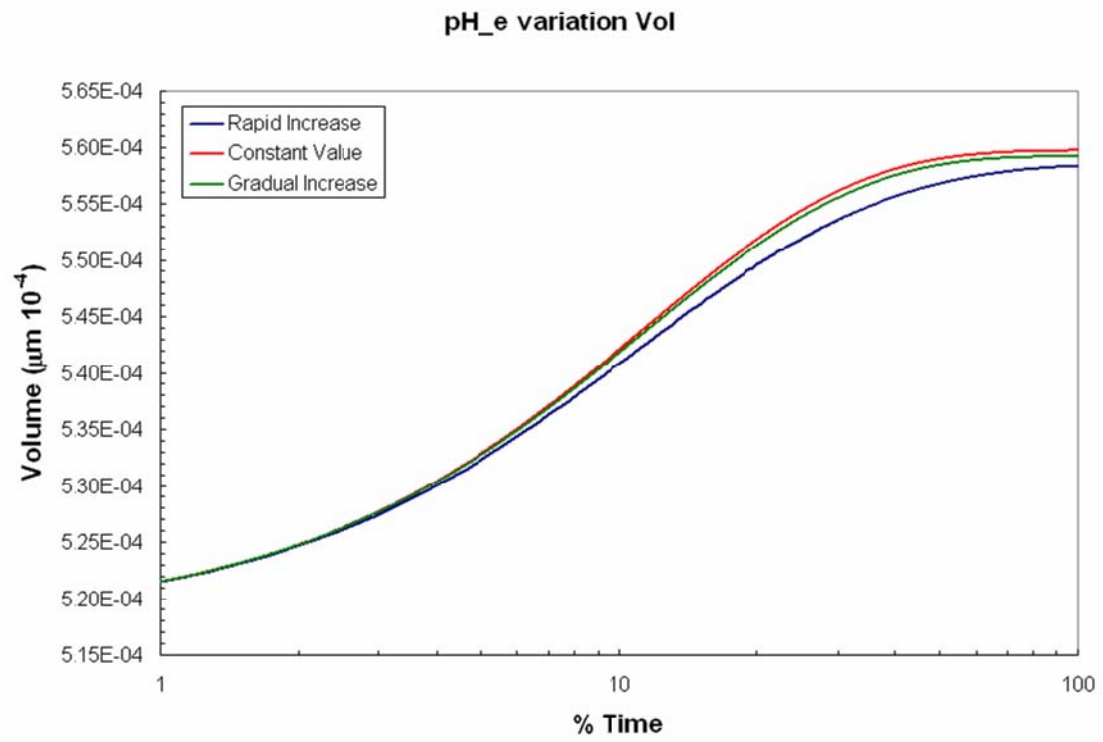
Figure 4-12 - Predicted volume response for each change in pH

5.0   PHARMACEUTICAL APPLICATIONS

5.1 NASTIC POSSIBILITIES

While nastic research to date has, by definition, focused on mimicking plant motions, all biological systems utilize various combinations of transport proteins penetrating a phase-separating bilayer membrane. Because the modeling construct developed as part of this research is generalized it could therefore be directly adapted to phenomena specific to the animal kingdom. One particularly intriguing adaptation includes applying the nastic modeling concept to the creation of highly targeted drug or vaccine delivery (though renaming of the model may be in order). In this scenario the inclusion will contain a species requiring delivery to a specific location within the body. The application emphasis switches from repeatable expansion/contraction of an actuator to that of controlled burst to release the payload as needed. While the discussions presented in this chapter are still preliminary, the example applications are compelling. These include but are not limited to:

- Delivery of a chemotherapy drugs specifically at the site of a tumor, with *no* release of this poison elsewhere in the body;

- Release of pain-mitigation or any repeat-need drugs as needed (this represents a significant improvement over time release technology that inappropriately assumes some average rate of need); and

- Delivery of DNA-based vaccines for anthrax, and even cancer with dramatically superior effectiveness as compared to that of the current norm of protein-based vaccines.

The thought process underlying these applications is this - because nastic inclusions exhibit an on-trigger response, the inclusions will be stimulated to expand only in the presence of some predetermined trigger. In the tumor example, that trigger would be found only at the location of the tumor. In the as-needed drug delivery, all inclusions would respond to rising concentrations of some trigger. But if the inclusions were designed to burst at different rates, then the first round of burst would neutralize the trigger preventing further drug release. As seen in the studies of varied ATP and pH stimulus, it is possible to design the inclusions such that the remainder will 'pump back down,' as the trigger diminishes. Similarly with the next round of release after the first round runs it course.

In the case of vaccine delivery, a natural pH driven process known as endocytosis tends to degrade the vaccine prior to delivery at an appropriate intracellular location; in this case a quantifiable model projecting how variations in the chemical state interior to the inclusion to combat this process will enable release of a fully functional payload. The following discussion and case study are still preliminary; the intent is to establish basic suitability of the nastic membrane model for projecting performance of drug/vaccine delivery strategies.

## 5.2 THE ROLE OF ENDOCYTOSIS IN VACCINE DELIVERY

The anthrax incidents in the Fall of 2001 underscored current vulnerability to organized assaults with biological weapons. The relatively small initial amount of anthax spores may have

exposed up to 30,000 people, resulting in 5 deaths. In a more organized assault with aerosol form, the attack could be far more fatal.

While a vaccine for Anthrax was developed in 1970, this vaccine led to complaints of reactogenicity (the capacity of a vaccine to produce adverse reactions/side effects) among its users. Several new delivery systems for the vaccine are currently being considered. One of the more promising techniques involves the intracellular delivery of peptides via genetic fusion with anthrax tocin. The success of this strategy hinges on developing a better understanding of the mechanism by which the vaccine reaches the cell nucleus, namely endocytosis. (Brey, 2005)

Similarly, the current proposed method for developing a viable cancer treatment involves introducing DNA based vaccines directly to the nucleus of affected cells. (Luo, Saltzman 2000). The vaccine is absorbed into the cell through the process of endocytosis. In this process the cell extends and surrounds the vaccine for intake; the vaccine is then enclosed in an inclusion type known as an endosome. With the foreign species safely encased (similarly for a virus DNA or vaccine DNA), this endosome is then transported to the interior of the cell (Figure 5-1). While the endosome provides a convenient mode of transport for uptake, it also acts to destroy and break down its contents before releasing it into the cell through pH driven process. This natural process tends to protect us from viruses, but serves as a barrier to successful DNA vaccine delivery. The vaccine must have some mechanism to release itself from the endosome before significant degradation occurs. Further, after the vaccine escapes from the endosome, it must then make its way to the nucleus and deliver the treatment.
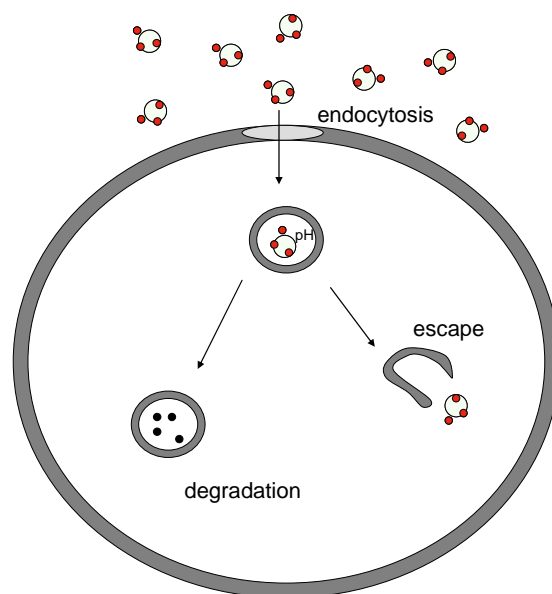
Figure 5-1 – Endocytosis

Therefore there are three major obstacles to this method of drug delivery. The first challenge lies with the low rate of intake across the cell membrane. While the vaccine may reach the outer cell wall, the cell itself must absorb the vaccine into the endosomes before it can be utilized. This rate of uptake may be increased through several treatments, the most promising of which is chemical treatments. (Luo, Saltzman, 2000)

The second challenge lies in escaping from the endosome itself. The endosome typically has a low internal pH value, and is designed to break down and degrade the contents before releasing them to the interior of the cell. Because these endosomes by nature contain a low pH, it may be possible for this low pH to serve as a trigger for the expansion of the inclusions. With sufficient expansion the endosome will burst prior to the onset of degradation of the contents. This is a challenge well suited to the capabilities of the nastic modeling strategy.

The third challenge is lack of nuclear targeting. Assuming that the DNA makes it through the endosome unscathed, it still must successfully locate the nucleus of the cell and

deliver the vaccine. This too could ultimately be studied via the nastic modeling construct. The previous challenge mandates early release of the endosome contents; this challenge mandates an optimization of 'how early.'

With the basic endocytosis process defined, consider next some details of how it occurs.

Endosomes are the natural inclusions formed at the outer cell surface which take in and absorb material to be sorted and processed. Despite considerable levels of interest, little information is known on the exact workings of theses inclusions.

During endocytosis, it has been observed that the inner pH of the endosome rapidly acidifies to 5 ± 0.2. (Yamashiro et al. 1983). As the endosome travels down its channel, the internal pH will vary between 5-6 (Beaumelle, Hopkins, 1989). The mechanism for this acidification has been found to be ATP powered proton pumps which supply a constant influx of H+. The endosomes use this internal pH to separate the ligands from their receptors, degrade the encased contents, then send the receptors back outside of the membrane while degrading the ligands. Through this the cell recycles the receptors and safely sorts the ligands that it receives.

While much of the process is still unknown, it has been observed that endosomes themselves lack a cohesive shape or structure. The endosomal compartments involved in intracellular processing includes a very diverse collection of vesicular and tubular elements. The common trait of these endosomes is that the acidic pH in endosomes plays a critical role in mediating the orderly traffic of the receptors and ligands during the endocytosis process (Fuchs et al. 1988, Bramwell et al. 2004). Moreover, it has been established that ATP proton pumps are responsible for pH regulation, and that the small size of the endosomes enables the ATP pumps to maintain the pH required for this natural process. (Fuchs et al. 1988) .

A maximum pH gradient exists, as adding additional ATP to an already acidized endosome does not increase the acidity. Also, the membrane permeability of the endosome is sufficient to stabilize a transmembrane pH gradient via an electrochemical potential (the membrane leaks ions). Therefore, the endosomal proton pumps are electrogenic (create a new flow of charge across the membrane).

These endosomes provide an interesting problem with delivering immunogenic proteins for immunity. Endosomes will naturally sort and degrade the vaccines unless the protein is able to escape the endosomes before complete degradation occurs. Currently, large amounts of the vaccine proteins are not delivered to the nucleus and are degraded to the point of uselessness. Through further studies and modeling of the endocytosis process, the amount of vaccine degraded may be reduced.

The foregoing discussion draws attention to a number of critical obstacles faced in the successful implementation of DNA-vaccine delivery that could be assessed via the nastic modeling construct. These issues include: the variations in endosome geometry, the importance of being able to quantify or even control the internal pH and rate of ATP proton pumping to prevent vaccine degredation, and the role of membrane properties including permeability and mechanical integrity. The following section offers a simple study on the role of geometry in inclusion (endosome) burst.
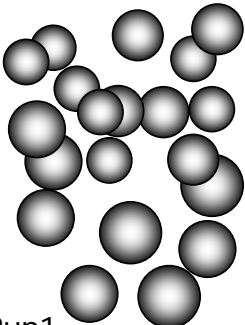
5.3 BURST PROFILES

In order to understand the role of geometry in burst, a number of spherical sizes are considered simultaneously. The nastic components are ideally triggered by an external source,
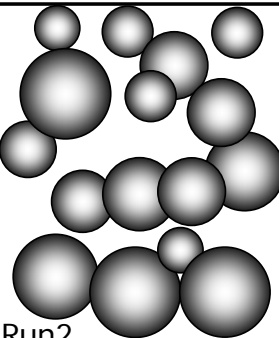
causing them to expand and eventually burst through gradually increasing surface area strain. The rate of inclusion content release through staggered burst rates would be important, as only the required amount of material should be released. This method of delivery is separate from the endocytosis mechanism, yet these principles may be beneficial in further studies.
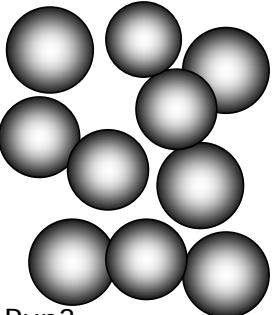
For this study, the surrounding solid material is modeled as a cube. For this preliminary study of the applicability of the nastic modeling construct for the projection of pharmaceutical burst profiles a completely spherical casing would be more physically accurate. However, burst is projected per a maximum surface strain criterion which necessarily occurs at the thinnest region of the solid cross-section, and is relatively insensitive to the existence of thicker regions. Similarly, exact material burst properties are not available and thus the articificial membrane material properties are employed; this would tend to impact the exact time at which burst is predicted to occur, but the generalized trends will remain the same. The prediction times are therefore normalized.

The burst rate study employs geometry ratios; to achieve this, the original model is modified to incorporate a large range of different radii and distributions thereof, while maintaining the same membrane thickness. By varying both inclusion size and distribution of inclusion size, average time to burst is obtained through the area strain ratio. Projection of the burst profile required monitoring the predicted inclusion volume with respect to time in the simultaneous solution of equations; a specified burst strain of 1.2% is employed. This value is arbitrary but consistently employed to explore trends. Results are reported in terms of the percent of inclusion contents (volume) released for the total distribution of inclusions with respect to time (normalized with respect to total time in the absence of experimental validation).

The time to burst for each model was determined through a program written in visual basic embedded into Excel. This program is able to search through each of the space-delineated output files created by the UFLUID program and determine when the specified area strain was reached through comparing the initial volume to the current volume and calculating the strain from those values. After this strain was reached, the program reports the current value of time and continues onto the next model to check.

Radius(10^{-8}) m	%comp
8	25.00
9	25.00
10	25.00
11	25.00
12	0.00
13	0.00
14	0.00
15	0.00
16	0.00

Run1

Radius(10^{-8}) m	%comp
8	11.11
9	11.11
10	11.11
11	11.11
12	11.11
13	11.11
14	11.11
15	11.11
16	11.11

Run2

Radius(10^{-8}) m	%comp
8	0.00
9	0.00
10	0.00
11	0.00
12	0.00
13	0.00
14	10.00
15	40.00
16	50.00

Run3

Figure 5-2 – Illustration of Various Compositions

For these burst profiles, 9 different geometries were considered with radii ranging from 8×10^{-8} m to 16×10^{-8} m. Each one of these geometries was simulated through UFLUID under baseline conditions, with the conditions scaled by the new surface areas and volumes for the different inclusions. The volume predictions from each of these simulations were used to determine the length of time until the specified burst strain was reached. Three geometry compositions were created as seen in figure 5-2, with varying concentrations of the different inclusions. These compositions were combined with the time to burst strain to create the burst prediction plot below. The significance of this result is that considerable control over the release profile of the enclosed species exists simply via varying the inclusion size. Other control parameters include transporter density per unit surface area and concentration of ATP or similar stimulus used by the specified pumps.
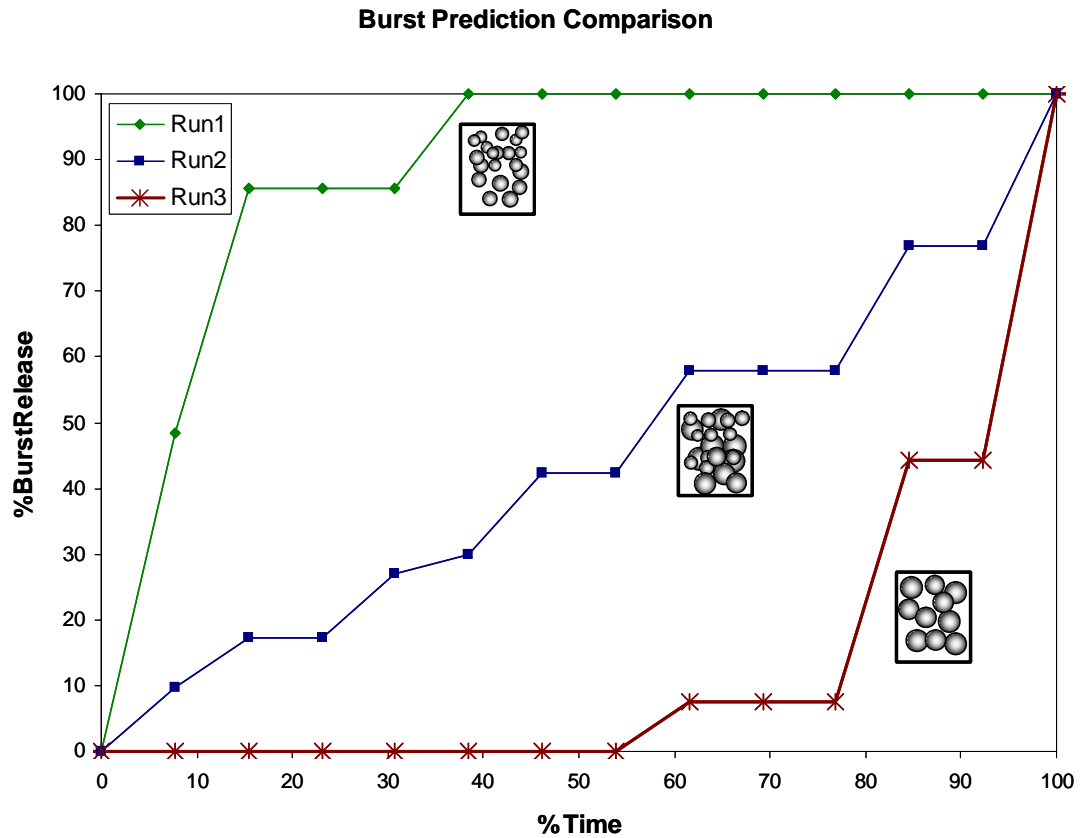
Figure 5-3 – Compilation of Different Burst Profiles.

As these burst profiles demonstrate, inclusion geometry likely plays an important role in burst. Smaller radii were observed to initially expand more rapidly than the larger radii with an initial acceleration, but the overall increased performance of the larger inclusions rapidly overtook the smaller inclusions expansion as time went on. Therefore, specified burst strain is of considerable interest, because if a high value of strain is employed the larger inclusions will actually burst first. If a low value of strain is considered, the opposite is true. Membrane thickness may also play a large part in this study.

6.0   CONCLUSIONS

Nastic materials use a combination of hyperelastic and transport concepts to achieve bulk deformation and are capable of producing significant deformation and blocked force.   The membrane examined in this research contains pumps, cotransporters, and exchangers embedded in a polymer matrix which provides resistance to the deformation.   The behavior of the nastic material is calculated through a combination of ABAQUS for the surrounding polymer and UFLUID for solving the stiff system of ODEs for the driving transport processes.

Through modifying the geometry of the inclusion, it was found that reducing the amount of surrounding polymer volume results in a much more relaxed behavior of the inclusion.   The initial expansion is still dominated by the transport processes; however the behavior after the expansion is altered drastically by the reduction.   Because the reduced surrounding polymer volume provides much less resistance to the deformation, the fluid is forced through the membrane at a much lower rate, allowing the inclusion to remain at peak volume for a much longer period of time.   This results in a much lower peak pressure, with a slightly higher peak volume and a longer period of time at the peak volume.

To check this behavior the permeability of the membrane was also varied.   It was found that the behavior of the inclusion after initial expansion was controlled largely by the amount of fluid forced out through the permeable membrane, as lower values of permeability resulted in significantly longer amounts of time at expanded volume.   The rate of diffusion was strongly impacted by the characteristics of the nastic membrane, as well as the amount of surrounding polymer volume.

Values for blocked force and free displacement were also estimated for these studies. It was found that the geometry cases with higher R/L ratios had much lower work done at the internal membrane, however the amount of work transmitted to the surroundings improved drastically as the amount of surrounding polymer volume decreased. This indicates that reduction of surrounding polymer volume results in a more efficient transmission of work to the surroundings.

Nastic materials were also considered for possible use in pharmaceuticals. They would offer a unique solution to targeted delivery of vaccines because of the triggered nature of the nastic inclusion. The concept for the study came from the possibility of inserting specifically tailored nastic inclusions into the bloodstream which would expand when coming into contact with an external stimulus and eventually burst, releasing the contents and neutralizing the stimulus. This research is still in early phases of development, and little is known on the conditions that the nastic inclusion would weather during injection and burst, so initial studies were conducted to determine the possibility.

For burst delivery to be a possibility, the inclusions would have to burst at different rates to ensure that the entire group did not burst and waste excess vaccine. The simplest method to control burst would be through altering the geometry of the inclusions. Plots of burst release were created for different mixes of varying inclusion geometries, and it was found that burst control would be possible through this method.

Further studies were necessary to determine whether or not the expansion process would be reverted by the consumption of the surrounding stimulus. In the current model, the stimulus is the availability of ATP. It was found that changing the amount of available ATP resulted in a

rapid change in inclusion behavior, which indicated that the burst process could be reversed if the stimulus had been neutralized.

Endocytosis seems to be the most likely candidate for delivering the vaccine to the cell nucleus. More research on this is needed, but prelimary studies were performed to check the behavior of the nastic inclusions in an environment with a changing pH value. It was found that the inclusion performance was affected minimally by the changing environment present during cell uptake.

These results show that the nastic material holds promise for pharmaceutical delivery along with actuation applications. The results in this thesis bode well for future nastic development, and nastic materials may be a versatile solution to many engineering problems.

7.0   FUTURE WORK

Currently more research is required into the burst delivery concept. For instance, a broader range of geometries should be considered. Also, when dealing with rupture mechanics hyperelastic assumptions may require reconsideration.

The model may be improved through the implementation of an advanced elasticity approach. The membrane will be modeled as a spherical shell using the appropriate strain energy potential equation. This will allow for a more flexible model of the bilayer membrane itself, along with the capability of modeling surrounding materials and applied conditions, such as flow over the membrane, contact with other membranes, and the effect of surrounding the membrane with viscous fluid.

With this model, more accurate modeling of endocytosis may be possible. The current understanding of how the inclusions would be taken into the cell through endocytosis is limited – it is not certain whether the inclusion would have to burst both itself and the surrounding membrane, or whether the cell would ever absorb the inclusion initially. Controlled rupture of the endosomes will be difficult to achieve/model if the inclusions studied in the experiment are forced to rupture before uptake, and the model used for studying the nastic inclusions may be applied to model the endosomes rupture itself.

Other improvements may be possible through revisiting the underlying equations and examining the assumptions made. The current model assumes ideal operating conditions using a simple first order kinetics model. If the equations are modified to reflect a more appropriate

reaction process, the solution method may have to be changed as the system of equations will become increasingly nonlinear.

REFERENCES

ABAQUS Analysis User's Manual, Vols. II, III, IV, and VI,2004, ABAQUS, Inc., Providence, Rhode Island.

Beamelle, Bruno and Hopkins, Colin. 1989. "High yield isolation of functionally competent endosomes from mouse lymphocytes". Biochem J. Vol 264, pp 137-149.

Bonting, S. L., and de Pont, J. J. H. H. M., 1981, New Comprehensive Biochemistry Volume 2 – Membrane Transport, Elsvier, New York.

Bramwell, Vincent W, Eyles, Jim E., Alpar, H. Oya. 2005. "Particulate delivery systems for biodefense subunit vaccines." Advanced Drug Delivery Reviews, 57, pp 1247-1265.

Cadogan, David, Smith, Uhelsky, Frank, and MacKusick, Matt. "Morphing Inflatable Wing Development for Compact Package Unmanned Aerial Vehicles". 45th AIAA/ASME/ASCE/AHS/ASC Structures, Structural Dynamics and Materials Conference, Palm Springs, California, Apr. 19-22, 2004

Disalvo, A. Siddiqi, F. A., and Ti Tien, H, 1989. "Membrane Transport with Emphasis on Water and Nonelectrolytes in Experimental Lipid Bilayers and Biomembranes", In *Water Transport in Biological Membranes, Vol 1,* Benga G., ed., CRC Press, Inc., Boca Raton, FL, pp. 41-75.

Endresen, L. P., 1997, "Chaos in weakly-coupled pacemaker cells", J. Theor. Biol., 184, pp. 41 – 50.

Endresen, L. P., 2000, "Runge-Kutta formulas for cardiac oscillators", Institutt for fysikk, NTNU, N-7034 Trondheim, Norway.

Endresen, L. P., Hall, K., Høye, J. S., and Myrheim, J., 2000, "A theory for the membrane potential of living cells", Eur. Biophys. J., 29, pp. 90 – 103.

Freeman, Eric, and Weiland, Lisa, 2008. "Applications of Biologically Inspired Membranes", Proc of SMASIS, Oct 28-30, Ellicott City, MD.

Freeman, Eric, and Weiland, Lisa, 2007, "Parametric Studies of a Coupled Transport/Hyperelastic Model for High Energy Density Nastic Materials", Proc of ASME-IMECE, Nov 14-16, 2007, Seattle, WA.

Freeman, Eric and Weiland, Lisa, 2008. "High Energy Density Nastic Materials: Parameters for Tailoring Active Response". *In press*, Journal of Intelligent Material Systems and Structures.

Fuchs, Renate, Male, Phillipe, and Mellman, Ira. 1988. "Acidification and Ion Permeabilities of Highly Purified Rat Liver Endosomes." The Journal of Biological Chemistry, 264, pp 2212-2220.

Hodgkin, A. L., and Huxley, A. F., 1952, "A Quantitative Description of Membrane Current and its Application to Conduction and Excitation in Nerve", *J. Physiol.* (London), 117, pp. 500 – 544.

Hodgkin, A. L., Huxley, A. F., and Katz, B., 1952, "Measurement of Current-Voltage Relations in the Membrane of the Giant Axon of Loligo", *J. Physiol.* (London), 116, pp. 424 – 448.

Homison, C, 2006, "Coupled Transport/Hyperelastic Model for High Energy Density Nastic Materials", University of Pittsburgh Masters Thesis.

Homison, C. and Weiland, L. M., 2005, "Coupled Transport/Hyperelastic Model for Nastic Materials", Proc. Of ASME – ISME, Nov. 5 – 11, 2005, Orlando, FL.

Homison, C. and Weiland, L.M., 2006, "Coupled Transport/Hyperelastic Model for Nastic Materials," Proc. SPIE, San Diego, CA, March 2006

Jeerage, Kavita M, Noble, Richard D., and Koval, Carl A. 2007. "Investigation of an aqueous lithium iodide/triiodide electrolyte for dual chamber electrochemical actuators". *Sensors and Actuators B* 125, 2007, pp 180-188.

Luo, Don and Saltzman, W. Mark. 2000. "Synthetic DNA Delivery Systems." Nature Biotechnology, Vol 18.

Mathews, L, Sundaresan, V.B., Giurgiutiu, V, and Leo, D.J., 2006a, "Bioenergetics and mechanical actuation analysis with membrane transport experiments for use in biomimetic nastic structures," *J. Mater. Res*. 2006; 21(8); 2058-2067.

Mathews, L, Giurgiutiu, V. 2006b. "Modeling Actuation Forces and Strains in Nastic Structures". Smart Structures and Materials 2006: Smart Structures and Integrated Systems – SPIE, Volume 6173, pp. 502-511.

Mauck, Lisa D, and Lynch, Christopher H, 2000, "Piezoelectric Hydraulic Pump Development," *J. Intellligent Materials Systems and Structures*, 11, pp 758-764.

Mullins, L. J., 1977, "A Mechanism for Na/Ca Transport", *J. Gen. Physiol*., 70, pp. 681 – 695.

Mullins, L. J., 1981, *Ion Transport in Heart*, Raven Press, New York.

Newnham, R. E., 1992, "Piezoelectric Sensors and Actuators: Smart Materials", Prov of 46th IEEE Frequency Control Symposium, May 27-29, 1992, Hershey, PA, pp 513-524

Oates, W. S., Mauck, L. D., and Lynch, C. S., 2000, "PZT piston driven hydraulic pump development", Proc of 12th IEEE International Symposim on Applications of Ferroelectrics, Jul 21-Aug 2, 2000, Honolulu, HI, **2,** pp 733-736.

Philen, MK et al 2007. "Fibrillar Network Adaptive Structure with Ion-transport Actuation". *Journal of Intelligent Material Systems and Structures*. Vol 18, April 2007, pp 323-334.

Ries, R. S., Choi, H., Blunck, R., Beznilla, F., and Heath, J. R. 2004, "Black Lipid Membranes: Visualizaing the Structure, Dynamics, and Substrate Dependence of Membranes", J. Phys. Chem. B, **108**, pp 16040-16049

Robinson, R. A., and Stokes, R. H., 1965, *Electrolyte Solutions*, Butterworths, London.

Schultz, S. G., 1980, *Basic Principles of Membrane Transport*, Cambridge University Press, New York.

Stein, W. D., 1989, "Kinetics of Transport: Analyzing, Testing, and Characterizing Models Using Kinetic Approaches", In Methods in Enzymology Vol. 171, Part R, Transport Theory: Cell and Model Membranes, Abelson, J. N. and Simon, M. I., eds., Academic Press, San Diego, CA, pp 23-62.

Stein, W. D., 1986, *Transport and Diffusion across Cell Membranes,* Academic Press, Inc., Orlando, FL.

Su, Y., Lin, L., and Pisano, A., 2002, "A Water-Powered Osmotic Microactuator", *J. Microelectromechanical Systems*, 11(6), pp. 736 – 742.

Sundaresan, V. B. and Leo, D. J., 2007, "Biological Ion Transporters as Gating Devices for Chemomechanical and Chemoelectrical Energy Conversion", Virginia Polytechnic Institute and State University, Virginia.

Sundaresan, V.B., Homison, Chris, Weiland, L.M., and Leo, D.J., 2007, "Biological Transport Processes for Microhydraulic Actuation," *Sensors and Actuators B: Chemical,* Vol 123, Iss 2, 21 May 2007, pp 685-695 .

Sundaresan, V. B. and Leo, D. J., 2005, "Experimental Investigation for Chemo-Mechanical Actuation using Biological Transport Mechanisms". Proc of ASME-IMECE, Nov 5-11, 2005, Orlando, FL,.

Sundaresan, V. B. and Leo, D. J., 2006,b "Controlled Fluid Transport Using ATP-Powered Protein Pumps", *Smart Mater. Struct.* **16** S207-S213

Sundaresan, V. B., Tan, H., Leo, D. J., and Cuppoletti, J., 2004, "Investigation on High Energy Density Materials Utilizing Biological Transport Mechanisms", Proc. Of ASME – IMECE, Nov 15 – 21, 2004, Anaheim, CA, 69, pp. 55-62 A

Tzou, H S, Lee, H J, and Arnold, S M, 2004, "Smart Materials, Precision Sensors/Acutators, Smart Structures, and Structronic Systems", Mech. Adv. Mater. Struc., 11, pp 367-393

Yamashiro, Darrel, Fluss, Sharon R and Maxfield, Frederick, 1983. "Acidification of Endocytic Vesicles by an ATP-dependent Proton Pump". *J of Cell Biology*, Vol 97, pp 929-934